

# An interface capturing method for liquid-gas flows at low-Mach number



Federico Dalla Barba<sup>a</sup>, Nicolás Scapin<sup>c,\*</sup>, Andreas D. Demou<sup>c</sup>, Marco E. Rosti<sup>d</sup>,  
Francesco Picano<sup>b</sup>, Luca Brandt<sup>c,e</sup>

<sup>a</sup> CISAS, University of Padova, Padova, Italy

<sup>b</sup> Department of Industrial Engineering & CISAS, University of Padova, Padova, Italy

<sup>c</sup> Department of Engineering Mechanics, Royal Institute of Technology (KTH), Stockholm, Sweden

<sup>d</sup> Complex Fluids and Flows Unit, Okinawa Institute of Science and Technology Graduate University (OIST), 1919-1 Tancha, Onna-son, Okinawa 904-0495, Japan

<sup>e</sup> Department of Energy and Process Engineering, Norwegian University of Science and Technology (NTNU), Trondheim, Norway

## ARTICLE INFO

### Article history:

Received 16 May 2020

Revised 12 October 2020

Accepted 17 November 2020

Available online 3 December 2020

### Keywords:

Compressible multi-phase flows

Volume-of-Fluid method

Low-Mach number asymptotic expansions

Pressure-correction methods

## ABSTRACT

Multiphase, compressible and viscous flows are of crucial importance in a wide range of scientific and engineering problems. Despite the large effort paid in the last decades to develop accurate and efficient numerical techniques to address this kind of problems, current models need to be further improved to address realistic applications. In this context, we propose a numerical approach to the simulation of multiphase, viscous flows where a compressible and an incompressible phase interact in the low-Mach number regime. In this frame, acoustics are neglected but large density variations of the compressible phase can be accounted for as well as heat transfer, convection and diffusion processes. The problem is addressed in a fully Eulerian framework exploiting a low-Mach number asymptotic expansion of the Navier-Stokes equations. A Volume of Fluid approach (VOF) is used to capture the liquid-gas interface, built on top of a massive parallel solver, second order accurate both in time and space. The second-order-pressure term is treated implicitly and the resulting pressure equation is solved with the eigenexpansion method employing a robust and novel formulation. We provide a detailed and complete description of the theoretical approach together with information about the numerical technique and implementation details. Results of benchmarking tests are provided for five different test cases.

© 2020 Elsevier Ltd. All rights reserved.

## 1. Introduction

Multiphase flows of two or more immiscible and viscous fluids are common in a large variety of engineering applications and fundamental scientific problems. Each phase is segregated and gives origin to complex and time-evolving free boundaries where discontinuities in the flow fields exist [1]. The phases mutually interact exchanging mass, momentum and energy across the free boundaries, the latter undergoing large and complex deformations. It is therefore clear how the description of the problem is extremely challenging both from a theoretical and numerical point of view. Some of the major issues affecting the modeling of multiphase flows arise from the discontinuities in the flow variables and prop-

erties across the free boundaries, from the necessity of numerically tracking and reconstructing the interfaces as well as from the need to account for the effect of the surface tension and jump conditions at the interfaces. These aspects are critical in the simulations of incompressible and isothermal multiphase flows, but additional complexity is added when the compressibility needs to be taken into account. In the latter case, heat transfer between the fluid phases and the boundaries must be considered in addition to mutual heat transfer between the phases and density variations. In this paper, the emphasis is on the multiphase flows of two immiscible viscous fluids, one of them being compressible, the other being incompressible. The attention is paid in particular to the low-Mach number flows, where the effect of compressibility is significant and large density variations occur in the compressible phase while acoustics are negligible. This is of great interest for several applications. To mention some, the simulation of bubble-laden flows and boiling flows [2–4], as well as the simulation of

\* Corresponding author.

E-mail addresses: [federico.dallabarba@phd.unipd.it](mailto:federico.dallabarba@phd.unipd.it) (F.D. Barba), [nicolos@mech.kth.se](mailto:nicolos@mech.kth.se) (N. Scapin), [demou@mech.kth.se](mailto:demou@mech.kth.se) (A.D. Demou), [marco.rosti@oist.jp](mailto:marco.rosti@oist.jp) (M.E. Rosti), [francesco.picano@unipd.it](mailto:francesco.picano@unipd.it) (F. Picano), [luca@mech.kth.se](mailto:luca@mech.kth.se) (L. Brandt).

the fuel jet atomization processes in the combustion chambers of internal combustion engines [5,6].

A great amount of literature dealing with the numerical simulations of multiphase, viscous fluids has been produced [7–14]. Many approaches have been proposed both in the Eulerian and Lagrangian frameworks as well as hybrid methods. Among the latter, the arbitrary Lagrangian Eulerian (ALE) approach [15–17]. In this frame, interface-conforming grids are used where boundary conditions can be accurately prescribed on the free boundaries of the flow. The main advantage of the ALE methods is the accurate treatment of the interfaces. Nevertheless, the computational cost of this kind of simulations is large due to the adaptive mesh adjustment needed to preserve the conformity of the grid to the time-evolving interfaces. The need for re-meshing is removed in the frame of the fixed-Eulerian-grid methods. These are hybrid Eulerian-Lagrangian approaches also referred to as front-tracking methods [18]. The Immersed Boundary Method (IBM) belongs to this class of numerical techniques [19–21]. This approach consists in solving the governing equations for the flow on a fixed Eulerian grid while tracking the free boundaries separating the different phases of the flow by means of Lagrangian markers distributed over the interfaces. An additional forcing is imposed to the fluid, within a neighborhood of the interfaces, such that the boundary conditions are satisfied within a certain degree of accuracy. This class of methods have been successfully applied to the simulation of multi-phase flows [22,23]. Even if fixed-Eulerian-grid methods are computationally more efficient than conforming-grid methods, they suffer from low accuracy in the reconstruction and tracking of the interface. A popular alternative is the so-called front-capturing methods that are based on a fully Eulerian treatment of the interface tracking and reconstruction. These include essentially the Volume Of Fluid (VOF) method and the Level-Set Method (LSM). The LSM uses a continuous level-set function, usually the signed distance to the interface, to distinguish between the different phases of the flow [24–28]. Interfaces are accurately defined by an assigned level of the level-set function while the advection of the level-set function itself allows for an accurate tracking of the interfaces. In the LSM framework the interface curvature can be computed easily and accurately, nevertheless, these are not mass-preserving methods. Indeed, the advection of the level-set function may result in a mass loss or gain. The Volume-of-Fluid method [1,29–31], instead, uses a discontinuous colour function to represent each different phase separately, providing the potential to conserve mass at a discrete level and to accurately represent the interface topology. This is in general accomplished with an interface reconstruction procedure which can be either geometrical or algebraic. The former is based on approximating each portion of the fluid interface with a plane, as done in the Piecewise Linear Interface Calculation (PLIC) [32], while the latter consists in employing a suitable function to approximate the phase indicator. Common and established choices of the reconstructing function are the hyperbolic tangent from which the THINC [33] and MTHINC [34] methods are derived or simpler polynomial functions designed to locally reconstruct the phase indicator [35]. In both cases, the chosen function is also employed to compute the numerical fluxes of the interface advection equation.

A major part of the numerical approaches to the simulation of multiphase flows reported by archival literature and referenced above were originally developed for incompressible flows. A great effort has been spent in the last decades to extend these methods to the simulation of compressible multiphase flows [36–40]; nonetheless this is still a very active area of research. Among compressible flows, low-Mach number flows are of great interest for many applications where large density variations occur at low speeds, low subsonic regimes. When addressing the simulation of this flow regime, a central issue arises from the limitation imposed

on the time step by the fastest dynamics of the flow. Indeed, in a compressible flow the speed of propagation of pressure waves scales as  $1/Ma$ ,  $Ma$  being the Mach number. Many solutions to this problem have been proposed, such as an implicit treatment of the acoustic pressure [41,42]. Nevertheless, if the case under examination is dominated by free or forced convection where the amount of energy carried by the acoustics is only a small fraction of the overall energy of the flow, a low-Mach number asymptotic formulation of the Navier-Stokes equations can be used to numerically address the problem. Large density variations can be accounted for, completely neglecting acoustics, but still describing entropy and vorticity modes as well as taking into account compressibility [43,44]. In this frame, the pressure is split into two different terms: a zero-order, thermodynamic pressure,  $p_0$ , and a second-order pressure,  $p_2$ . The former is governed by the thermodynamic properties of the flow while the latter enters the computation in a similar fashion to that of pressure in incompressible flows [43].

In this context, we propose a one-fluid fully Eulerian approach to the numerical simulation of multiphase low-Mach number flows, based on the solution of a low-Mach number asymptotic formulation of the compressible Navier-Stokes equations. For the reconstruction and subsequent advection of the interface between the compressible and incompressible phases, we adopt an algebraic Volume-of-Fluid method (MTHINC [34]). However, the mathematical and numerical framework can be extended in a straightforward manner to any kind of interface capturing and tracking technique based on the sharp interface approach. The proposed method is implemented in the frame of the pressure-correction methods, taking advantage of a Fast-Fourier-Transform (FFT) based solver for the Poisson equation governing the second-order-pressure of the flow. The effect of the surface tension is accounted for by using the continuum surface force (CSF) model by Brackbill [45]. The implementation is built upon an extensively validated code for the simulation of incompressible flows. The solver uses second order finite difference schemes for space discretization on a fixed Eulerian grid and a second order of accuracy Adams-Bashforth time-marching algorithm [12,46–48]. While providing detailed and complete description of the theoretical approach together with information about the numerical technique and implementation details, we highlight how the first order pressure  $p_0$  should be computed in order to ensure mass conservation of the compressible phase and how to ensure that the constrain on the velocity divergence is correctly imposed. Because of its numerical efficiency, we believe that this approach is one of the most promising to efficiently address the simulation of multiphase, low-Mach number flows, in particular when one of the two phases can be assumed to be incompressible.

## 2. Governing equations

This section provides the derivation of the monolithic system of partial differential equations that governs the flow of two immiscible viscous fluids, one being compressible, the other being incompressible, e.g. a liquid-gas system. The regions of space occupied by the gas and the liquid phase,  $\Omega_g(t)$  and  $\Omega_l(t)$ , are assumed to be separated by a zero-thickness and time-evolving interface,  $S(t) = \Omega_g(t) \cap \Omega_l(t)$ . A phase indicator function,  $H(\mathbf{x}, t)$ , is defined to distinguish between the two phases,

$$H(\mathbf{x}, t) = \begin{cases} 1 & \text{if } \mathbf{x} \in \Omega_g(t), \\ 0 & \text{if } \mathbf{x} \in \Omega_l(t). \end{cases} \quad (1)$$

The dynamics of the liquid phase are assumed to be governed by the standard, incompressible Navier-Stokes equations. Since the framework is well-established [29], details are omitted here. On the other hand, the compressible phase is assumed to evolve in

the low-Mach number regime. The governing equations for a compressible, low-Mach number flow rely on a well-established framework too [44]. Nonetheless, the derivation of the low-Mach number model is presented in this section and in Appendix A to clarify the basic assumptions and range of validity of the monolithic approach presented in this paper.

### 2.1. Governing equations for the compressible phase

This subsection focuses on the compressible gas phase alone; all the quantities defined here refer only to the gas phase unless otherwise stated. In general, if compressibility is taken into account, a gaseous flow can be described by the following Navier-Stokes and energy equations:

$$\frac{\partial \rho}{\partial t} + \nabla \cdot (\rho \mathbf{u}) = 0, \quad (2)$$

$$\frac{\partial (\rho \mathbf{u})}{\partial t} + \nabla \cdot (\rho \mathbf{u} \otimes \mathbf{u}) = \nabla \cdot \boldsymbol{\tau} - \nabla p + \mathbf{f}_\sigma + \rho \mathbf{g}, \quad (3)$$

$$\begin{aligned} \frac{\partial (\rho e_t)}{\partial t} + \nabla \cdot (\rho \mathbf{u} e_t) = \nabla \cdot (\boldsymbol{\tau} \cdot \mathbf{u}) + \nabla \cdot (k \nabla T) \\ - \nabla \cdot (\rho \mathbf{u}) + (\mathbf{f}_\sigma + \rho \mathbf{g}) \cdot \mathbf{u}, \end{aligned} \quad (4)$$

$$p = \rho \mathcal{R} T, \quad (5)$$

where  $\mathbf{u} = (u, v, w)$ ,  $\rho$  and  $p$  are the fluid velocity, density and pressure,  $\mathbf{g}$  is the gravitational acceleration and  $k$  the thermal conductivity. The specific total energy of the flow,  $e_t = e + \mathbf{u} \cdot \mathbf{u}/2$ , includes the specific internal energy,  $e$ , and the specific kinetic energy,  $\mathbf{u} \cdot \mathbf{u}/2$ . The Newton-Stokes constitutive relation is assumed to hold, such that the viscous stress tensor is

$$\boldsymbol{\tau} = \mu \left[ (\nabla \mathbf{u} + \nabla \mathbf{u}^T) - \frac{2}{3} (\nabla \cdot \mathbf{u}) \mathbf{I} \right], \quad (6)$$

with  $\mathbf{I}$  the identity tensor and  $\mu$  the dynamic viscosity. The effect of the surface tension on the interfaces separating the incompressible and compressible phases is modeled by a continuum surface force, (CSF) [45]:

$$\mathbf{f}_\sigma = \sigma \kappa \delta(\mathbf{x} - \mathbf{x}_s) \mathbf{n}, \quad (7)$$

where  $\sigma$  is the surface tension coefficient,  $\kappa$  the curvature of the interface and  $\mathbf{n}$  the unit normal on the interface pointing towards the compressible phase. A delta function,  $\delta(\mathbf{x} - \mathbf{x}_s)$ , is used in Eq. (7) to impose the force density,  $\mathbf{f}_\sigma$ , only at the interface position  $\mathbf{x}_s$ . We consider here an ideal-gas with equation of state (5). The parameter  $\mathcal{R}$  is the specific gas constant,  $\mathcal{R} = R/\mathcal{M}$ , where  $\mathcal{M}$  is the molar mass of the gas and  $R = 8.314 \text{ J}/(\text{mol} \cdot \text{K})$  the universal gas constant. Extending the model to deal with non-ideal equations of state, such as the Van der Waals equation or cubic equations of state [49], is straightforward, as these terms will enter the thermodynamic derivatives. Nonetheless, for the sake of simplicity, the discussion is limited to the use of Eq. (5). Moreover, we assume a calorically-perfect gas, e.g. the constant-pressure and constant-volume heat capacities,  $c_p$  and  $c_v$ , do not depend on the thermodynamic pressure and temperature. Eqs. (2)–(5) can be recast in non-dimensional form by setting as independent reference scales the density,  $\tilde{\rho}$ , the pressure,  $\tilde{p}$ , the length,  $\tilde{L}$ , the velocity,  $\tilde{U}$ , together with the following derived quantities:

$$\tilde{T} = \tilde{p}/(\mathcal{R} \tilde{\rho}), \quad \tilde{t} = \tilde{L}/\tilde{U}, \quad \tilde{e} = \tilde{p}/\tilde{\rho}, \quad \tilde{f} = \tilde{\rho} \tilde{U}^2/\tilde{L}.$$

The quantities above,  $\tilde{T}$ ,  $\tilde{t}$ ,  $\tilde{e}$  and  $\tilde{f}$  are the reference temperature, time, specific energy and force per unit volume. In addition, the reference values for the thermal diffusion coefficient, heat capacities, dynamic viscosity, surface tension coefficient and gravitational

acceleration are denoted as  $\tilde{k}$ ,  $\tilde{c}_p$ ,  $\tilde{c}_v$ ,  $\tilde{\mu}$ ,  $\tilde{\sigma}$  and  $\tilde{g}$ . Under the hypotheses specified above, the low-Mach number limit of Eqs. (2)–(5) can be derived by taking a single-scale asymptotic expansion in the limit of small Mach numbers [44] of their non-dimensional form. The related procedure is reported in details in Appendix A, while here we report the final form of the governing equations for the compressible phase:

$$\frac{\partial \mathbf{u}}{\partial t} + \mathbf{u} \cdot \nabla \mathbf{u} = \frac{1}{\rho} \left[ \frac{1}{Re} \nabla \cdot \boldsymbol{\tau} - \nabla p_2 + \frac{\mathbf{f}_\sigma}{We} \right] + \frac{\mathbf{g}}{Fr^2}, \quad (8)$$

$$\frac{\partial T}{\partial t} + \mathbf{u} \cdot \nabla T = \frac{T}{p_0} \left[ \frac{1}{RePr} \nabla \cdot (k \nabla T) + \frac{\gamma - 1}{\gamma} \frac{dp_0}{dt} \right], \quad (9)$$

$$\nabla \cdot \mathbf{u} = \frac{1}{p_0} \left[ \frac{1}{RePr} \nabla \cdot (k \nabla T) + \frac{1}{\gamma} \frac{dp_0}{dt} \right], \quad (10)$$

$$\frac{dp_0}{dt} = \frac{\gamma}{V} \left[ \frac{1}{RePr} \int_S k \nabla T \cdot \mathbf{n} dS - p_0 \int_S \mathbf{u} \cdot \mathbf{n} dS \right], \quad (11)$$

$$p_0 = \Pi \rho T, \quad (12)$$

where  $T$  is the temperature,  $Re = \tilde{\rho} \tilde{U} \tilde{L}/\tilde{\mu}$  the Reynolds number,  $Pr = \tilde{c}_p \tilde{\mu}/\tilde{k}$  the Prandtl number,  $We = \tilde{\rho} \tilde{U}^2 \tilde{L}/\tilde{\sigma}$  the Weber number and  $Fr = \tilde{U}/\sqrt{g \tilde{L}}$  the Froude number. The parameter  $\gamma = \tilde{c}_p/\tilde{c}_v$  is the specific heat ratio of the gas phase, whereas the constant  $\Pi$  is, by definition,  $\Pi = (\tilde{\rho} \mathcal{R} \tilde{T})/\tilde{p}$ . In Eq. (11), the volume  $V$  denotes the overall volume of the spatial region occupied by the compressible phase, whereas the surface integrals are computed along the boundaries of the latter. Two different pressure terms appear in Eqs. (8)–(12): the zeroth-order pressure,  $p_0$ , and the second-order pressure,  $p_2$ . The former, which can be referred to as thermodynamic pressure, is determined by the thermodynamic state of the flow, it is uniform across the spatial field and it is a function of the time only. The latter, conversely, enters the computation similarly to the pressure in incompressible flows (e.g. by imposing a prescribed value of the velocity divergence) and it is obtained as the solution of a Poisson equation, discussed in the following. It also worth remarking that, in the limit of small Mach number, the contribution of the viscous dissipation to the overall energy balance of the gaseous flow has been neglected. As addressed also in Appendix A, this holds true under the hypothesis of sufficiently high Reynolds number.

### 2.2. Final form of the governing equations

Eqs. (8)–(12) hold only for the compressible gas phase; these are coupled with those for the incompressible fluid by employing the phase indicator function defined in Eq. (1). Hence, a monolithic system of equations can be obtained, describing at the same time the dynamics of both the compressible and incompressible phases. For convenience, the system is written in dimensional form,

$$\frac{\partial \mathbf{u}}{\partial t} + \mathbf{u} \cdot \nabla \mathbf{u} = \frac{1}{\rho} (\nabla \cdot \boldsymbol{\tau} - \nabla p_2 + \mathbf{f}_\sigma) + \mathbf{g}, \quad (13)$$

$$\frac{\partial T}{\partial t} + \mathbf{u} \cdot \nabla T = \frac{1}{\rho c_p} \left[ \nabla \cdot (k \nabla T) + \frac{dp_0}{dt} H \right], \quad (14)$$

$$\nabla \cdot \mathbf{u} = \frac{1}{p_0} \left[ \frac{\gamma_g - 1}{\gamma_g} \nabla \cdot (k \nabla T) - \frac{1}{\gamma_g} \frac{dp_0}{dt} H \right], \quad (15)$$

$$\frac{dp_0}{dt} = \frac{\gamma_g}{V_g} \left( \frac{\gamma_g - 1}{\gamma_g} \int_S k \nabla T \cdot \mathbf{n} dS - p_0 \int_S \mathbf{u} \cdot \mathbf{n} dS \right), \quad (16)$$

$$p_0 = \rho \mathcal{R}T. \quad (17)$$

Eqs. (13)–(17) are consistent with those reported in Daru et al. [50]. The coefficients  $c_p$ ,  $k$  and  $\mu$  in Eqs. (13)–(17) should be intended as the heat capacity at constant pressure, thermal conductivity and dynamic viscosity of the bi-phase flow, respectively, whereas the parameter  $\gamma_g$ , which is meaningful for the gas phase only, is taken as a constant,  $\gamma_g = c_{p,g}/c_{v,g}$ . These quantities,  $k$ ,  $C_p$  and  $\mu$ , are computed, together with the density of the flow,  $\rho$ , by using the phase indicator function,  $H$ :

$$\rho = \rho_g H + \rho_l (1 - H), \quad (18)$$

$$c_p = c_{p,g} H + c_{p,l} (1 - H), \quad (19)$$

$$k = k_g H + k_l (1 - H), \quad (20)$$

$$\mu = \mu_g H + \mu_l (1 - H), \quad (21)$$

where the subscripts “g” and “l” refer to the physical parameter of the gas and liquid phases, respectively. While Eqs. (13)–(15) hold for both the phases, Eqs. (16) and (17) are meaningful for the compressible one, only. In particular, Eq. (15) reduces to  $\nabla \cdot \mathbf{u} = 0$  in the liquid regions, where  $H = 0$ .

As shown in Eq. (A.11), the zeroth-order pressure,  $p_0$ , is uniform inside each region occupied by the compressible phase. In each of these regions, the value of  $p_0$  is determined by the constitutive law for ideal gases (17), while its temporal rate of change is set by the energy balance provided by Eq. (16). In particular, the surface integrals appearing in Eq. (16) are computed over the interface,  $S$ , that separates the compressible and incompressible regions and, where necessary, over the boundaries of the computational domain. For numerical integration purposes, it is more convenient to reformulate Eq. (16) in terms of volume integrals, by employing the divergence theorem:

$$\frac{1}{p_0} \frac{dp_0}{dt} = \frac{\gamma_g}{V_g} \left( \frac{1}{p_0} \frac{\gamma_g - 1}{\gamma_g} \int_{\Omega} H \nabla \cdot (k \nabla T) dV - \int_{\Omega} H \nabla \cdot \mathbf{u} dV \right), \quad (22)$$

where the integrals are computed over the entire computational domain,  $\Omega = \Omega_g \cup \Omega_l$ , and  $V_g$  is the volume of the spatial region filled by the gas phase,  $\Omega_g$ . Eq. (22) can be derived by employing the change of variable,  $V_g = HV$ , with the related differential,  $dV_g = HdV$ , being  $dH = 0$  by definition of the phase indicator function [29].

### 3. Numerical methodology

The numerical solution of Eqs. (13)–(17) is addressed on a fixed regular Cartesian grid (e.g. using a uniform and equal spacing,  $\Delta x = \Delta y = \Delta z$ ), with a marker-and-cell arrangement of velocity and pressure points, whereas all scalar fields are defined at the cell centers. Hereafter, we present the numerical discretization of the governing equations following the same order in which they are solved.

#### 3.1. Interface representation and advection

The first step of each iteration of the time-marching algorithm consists in the reconstruction of the interface between the two phases and its subsequent advection. As mentioned in the introductory section, we address both the aspects in a fully Eulerian framework using the VOF method to distinguish between each of the flow phases [1]. By a numerical point of view the indicator

function  $H$ , defined in Eq. (1), is updated on the computational grid by the following advection equation:

$$\frac{\partial \Phi}{\partial t} + \nabla \cdot (\mathbf{u}H) = \Phi \nabla \cdot \mathbf{u}, \quad (23)$$

where the volume fraction,  $\Phi$ , is defined as the average value of the color function over a discrete computational cell of volume  $V_c = \Delta x \Delta y \Delta z$ :

$$\Phi = \int_{V_c} H(\mathbf{x}, t) dV_c. \quad (24)$$

Coherently with the given definition of  $H$  in Eq. (1), the volume fraction satisfies  $\Phi = 1$  in cells occupied by the gas phase only,  $\Phi = 0$  in that filled only by the liquid and  $0 < \Phi < 1$  in the cells containing the liquid-gas interface.

In the present work, we employ as VOF method the multi-dimensional tangent of hyperbola for interface capturing method (MTHINC), originally developed by Li et al. [34] and more recently applied to complex flows cases both in laminar [12,51,52] and in turbulent conditions [48]. The description of this VOF approach is not reported here as the present low-Mach algorithm is not limited to a specific interface capturing/tracking method; additional details on the MTHINC are provided in literature [12,34]. Once the interface is reconstructed, the advection step is performed using the standard directional splitting approach, originally developed by Puckett et al. [53] and Aulisa et al. [32]. Note that since there is no phase change, the one-fluid velocity is continuous and well-defined across the interface, therefore it can be employed as interface velocity in (23). Nevertheless, due to the thermal expansion/contraction in the gas phase,  $\mathbf{u}$  is not divergence free and, thus, the additional correction proposed in [54] is employed. This consists in adding, after the three directional splittings, a correction step proportional to the discrete velocity divergence:

$$\Phi_{i,j,k}^{n+1} = \Phi_{i,j,k}^{***} - \Delta t^{n+1} F_{i,j,k}^n + \Delta t^{n+1} \Phi_{i,j,k}^{n+1} (\nabla \cdot \mathbf{u})_{i,j,k}^n, \quad (25)$$

where  $\Phi_{i,j,k}^{***}$  is the volume fraction resulting from the directional splitting procedure,  $F_{i,j,k}^n$  represents the correction used in the standard directional-splitting method for a solenoidal advection velocity [34], and the last term represents a volume correction step that ensures that the non-zero velocity divergence is used to update  $\Phi_{i,j,k}^{n+1}$ .

Finally, the thermodynamic properties ( $\rho$ ,  $\mu$ ,  $k$  and  $c_p$ ) are updated using the relations (18)–(21).

#### 3.2. Temperature equation and thermodynamic pressure

The next step consists of the computation of the updated thermodynamic pressure  $p_0^{n+1}$  and temperature  $T^{n+1}$ . This last quantity is advanced using a second-order Adams-Bashforth time-marching algorithm:

$$T^{n+1} = T^n + \Delta t^{n+1} \left[ \left( 1 + \frac{1}{2} \frac{\Delta t^{n+1}}{\Delta t^n} \right) RT^n - \left( \frac{1}{2} \frac{\Delta t^{n+1}}{\Delta t^n} \right) RT^{n-1} \right]. \quad (26)$$

In the above,  $\Delta t^{n+1}$  and  $\Delta t^n$  represent the time step at time levels  $n + 1$  and  $n$ . The time step is chosen to fulfil the temporal stability requirements as explained in Section 3.4. The term  $RT$  is the right-hand side of the temperature Eq. (14), provided below in a semi-discrete notation:

$$RT^n = -\mathbf{u}^n \cdot \nabla T^n + \frac{1}{\rho^{n+1} c_p^{n+1}} \left[ \nabla \cdot (k^{n+1} \nabla T^n) + \left( \frac{dp_0}{dt} \right)^n \Phi^{n+1} \right], \quad (27)$$

where the rate of change of the thermodynamic pressure  $(dp_0/dt)^n$  is computed from Eq. (22) using  $T^n$ . All the spatial terms

in eq. (27) are discretized by second order central schemes, except for the temperature convection term. The discretization of the latter is based on the 5th-order WENO5 scheme as in reference [55].

Next, the thermodynamic pressure is updated. Here, different strategies are available. One possibility is to discretize (22) in time using for example the Adams-Bashforth method. Another approach, proposed in [50], is to integrate (22) in time to compute the new  $p_0$ .

$$p_0^{n+1} = p_0^n \exp \left( \int_{t^n}^{t^{n+1}} \frac{1}{p_0} \frac{dp_0}{dt} \Big|^{n+1} dt \right) \quad (28)$$

Nevertheless, both approaches are not built to satisfy as a key requirement the mass conservation of the compressible phase at a discrete level. When the gas density changes, the mass conservation cannot be fulfilled by the simple color function advection, which is only designed to ensure volume conservation. To overcome this issue, we adapt to our multiphase configuration the approach proposed by Motheau et al. [56] for combustion problems and more recently adopted by Demou et al. [57] for non-Boussinesq gravity currents. In this case, the calculation of  $p_0^{n+1}$  is performed by integrating the gas density Eq. (17) over the entire gas volume  $V_g$ ,

$$p_0^{n+1} = \frac{M_{g,t=0}}{\int_{V_g^{n+1}} \frac{1}{RT^{n+1}} dV_g^{n+1}}. \quad (29)$$

If the system is closed or periodic and no phase change occurs between the two phases, the gas mass is a constant, e.g.,  $M_g^{n+1} = M_{g,t=0}$ , and can be pre-computed at the beginning of the simulation. At each time-step,  $p_0$  is computed from Eq. (29) to satisfy exactly mass conservation of the compressible phase, and it therefore varies according to the global thermal expansion or contraction of the compressible phase. Note that the gas volume  $V_g^{n+1}$  over which Eq. (29) is integrated can be approximated as

$$V_g^{n+1} = \sum_{i=1}^{N_x} \sum_{j=1}^{N_y} \sum_{k=1}^{N_z} \Phi_{i,j,k}^{n+1} \Delta x \Delta y \Delta z, \quad (30)$$

where  $N_x$ ,  $N_y$  and  $N_z$  are the number of grid points along the  $x$ ,  $y$  and  $z$  directions.

### 3.3. Flow solver

In order to impose that the velocity field  $\mathbf{u}^{n+1}$  satisfies the divergence constraint given by Eq. (35), a pressure-correction scheme based on the Adams-Bashforth method is employed and summarized below in semi-discrete notation:

$$\mathbf{u}^* = \mathbf{u}^n + \Delta t^{n+1} \left[ \left( 1 + \frac{1}{2} \frac{\Delta t^{n+1}}{\Delta t^n} \right) \mathbf{R}\mathbf{U}^n - \left( \frac{1}{2} \frac{\Delta t^{n+1}}{\Delta t^n} \right) \mathbf{R}\mathbf{U}^{n-1} \right], \quad (31)$$

$$\nabla \cdot \left( \frac{1}{\rho^{n+1}} \nabla p_2^{n+1} \right) = \frac{1}{\Delta t^{n+1}} [\nabla \cdot \mathbf{u}^* - \nabla \cdot \mathbf{u}^{n+1}], \quad (32)$$

$$\mathbf{u}^{n+1} = \mathbf{u}^* - \frac{\Delta t^{n+1}}{\rho^{n+1}} \nabla p_2^{n+1}, \quad (33)$$

where  $\mathbf{u}^*$  is the predicted velocity. The right-hand side  $\mathbf{R}\mathbf{U}^n$  is computed as:

$$\mathbf{R}\mathbf{U}^n = -\mathbf{u}^n \cdot \nabla \mathbf{u}^n + \frac{1}{\rho^{n+1}} [\nabla \cdot \boldsymbol{\tau}(\mu^{n+1}, \mathbf{u}^n) + \mathbf{f}_\sigma^{n+1} + \rho^{n+1} \mathbf{g}], \quad (34)$$

where both the convection and diffusion terms are discretized by central schemes. More specifically, the former is discretized in divergence form as  $\nabla \cdot (\mathbf{u}\mathbf{u}) - \mathbf{u}\nabla \cdot \mathbf{u}$  whereas the latter is treated in

a fully conservative form. The surface normal vector  $\mathbf{n}$  and the curvature  $\kappa$  are obtained directly from the corresponding definitions, e.g.,  $\mathbf{n} = \nabla \Phi / |\nabla \Phi|$  and  $\kappa = \nabla \cdot \mathbf{n}$ , where the color function gradients are estimated directly with Youngs' method [58,59]. Finally, the divergence constraint in Eq. (32) is computed directly as

$$\nabla \cdot \mathbf{u}^{n+1} = \left[ \frac{1}{p_0^{n+1}} \frac{\gamma_g - 1}{\gamma_g} \nabla \cdot (k^{n+1} \nabla T^{n+1}) - \frac{1}{\gamma_g} \left( \frac{1}{p_0} \frac{dp_0}{dt} \right)^{n+1} \right] \Phi^{n+1}. \quad (35)$$

Note that the evaluation of the term  $(dp_0/dt)^{n+1}/p_0^{n+1}$  in (35) is performed directly with Eq. (22) using  $T^{n+1}$ ,  $k^{n+1}$  and  $\Phi^{n+1}$ .

#### 3.3.1. Pressure equation

A key feature of any two-fluid solver is the ability to impose accurately and efficiently the divergence constraint on the velocity field, this task being directly related to the numerical procedure used to solve the pressure equation, Eq. (32). A possible approach is based on the use of iterative multigrid solvers. Despite the success and the widespread use of these solvers, the solution is not exact, but satisfied up to a controlled tolerance, usually of the order  $\varepsilon = 10^{-7} - 10^{-8}$ . Moreover, since the coefficients of the Poisson equation vary in space, the system matrix must be recomputed at each time-step. Alternatively, when the pressure boundary conditions are homogeneous [60], a possible solution is to transform Eq. (32) into a constant coefficient equation and apply the method of the eigenexpansion [61,62] to solve the pressure equation exactly with spectral accuracy. The resulting pressure equation is still to be solved in an iterative manner starting with an initial guess. Different methods based on the latter approach are available in literature, the main difference being how the variable coefficient pressure equation is recast into a constant coefficient problem. In the following, we review two of these methods, that have been recently proposed and designed to efficiently solve in an iterative manner the Poisson equation with the method of eigenexpansion. It should be noted that, these methods have been successfully implemented in numerical codes that share with our one a similar parallelization strategy based on the **2DECOMP&FFT** [63] library. Finally, we will introduce a new methodology that proves to be more efficient and suitable for two-phase flows with capillary effects and sharp gradients between the two phases.

- Method I: this method has been proposed by Motheau and Abraham [56]. It is designed for low-Mach number reactive flows, aiming at decreasing the number of iterations of the previously developed FFT-based solvers for combustion applications. The methodology consists in a semi-implicit approach that first requires an iterative procedure to solve the following constant coefficient Poisson equation:

$$\nabla^2 p_2^{s+1} = \nabla \cdot \left[ \left( 1 - \frac{\tilde{\rho}_0^{n+1}}{\rho^{n+1}} \right) \nabla p_2^s \right] + \frac{\tilde{\rho}_0^{n+1}}{\Delta t^{n+1}} (\nabla \cdot \mathbf{u}^* - \nabla \cdot \mathbf{u}^{n+1}), \quad (36)$$

where,  $p_2^{s+1}$  and  $p_2^s$  are the hydrodynamic pressure at two subsequent iterations and  $\tilde{\rho}_0^{n+1}$  is the minimum value of  $\rho^{n+1}$  over the computational domain. After the iterative loop to compute  $p_2^{n+1}$ , a modified correction step is applied:

$$\mathbf{u}^{n+1} = \mathbf{u}^* - \Delta t^{n+1} \left[ \frac{1}{\tilde{\rho}_0^{n+1}} \nabla p_2^{n+1} + \left( \frac{1}{\rho^{n+1}} - \frac{1}{\tilde{\rho}_0^{n+1}} \right) \nabla p_2^{n+1,q} \right], \quad (37)$$

where  $p_2^{n+1,q}$  is the second-to-last hydrodynamic pressure of the iterative procedure at the new time-level. The main advantage of this method is the ability to effectively impose the velocity divergence up to machine accuracy, by setting a residual threshold to solve Eq. (36) to  $\varepsilon_t = 10^{-6} - 10^{-8}$ , being the

residual  $\varepsilon = ||p_2^{s+1} - p_2^s||$ ). Nevertheless, we find that using this approach in the case of a rising bubble (see Section 4.2), the number of iterations required to achieve convergence is of the order of one hundred.

- Method II: this approach, proposed by Bartholomew and Laizet [64] and designed for non-Boussinesq gravity currents, is based on the rearrangement of Eq. (32) as a constant coefficient Poisson equation:

$$\nabla^2 p_2^{s+1} = \nabla^2 p_2^s + \tilde{\rho} \left[ \frac{1}{\Delta t^{n+1}} (\nabla \cdot \mathbf{u}^* - \nabla \cdot \mathbf{u}^{n+1} - \nabla \cdot \frac{1}{\rho^{n+1}} \nabla p_2^s) \right], \quad (38)$$

where  $p_2^{s+1}$  and  $p_2^s$  are the hydrodynamic pressure at two subsequent iterations. Eq. (38) is solved in an iterative manner until convergence. After that, the correction step (33) is performed to obtain the new velocity field  $\mathbf{u}^{n+1}$ . The modified density  $\tilde{\rho}$  is taken as the harmonic mean between  $\rho_l$  and  $\rho_g$ , as suggested by the authors to improve convergence. To satisfy the divergence constraint up to machine accuracy, the threshold residual should be set to  $\varepsilon_t = 10^{-12}$ . In Section (4.2) we will show that this approach requires a lower number of iterations than the previous one, but still higher than the one we are going to present next.

- Method III: the basic idea behind this third approach, proposed here, is to rearrange the Poisson equation into a constant-coefficient form by employing the correction step (33):

$$\frac{1}{\rho^{n+1}} \nabla^2 p_2^{n+1} + \nabla \left( \frac{1}{\rho^{n+1}} \right) \cdot \nabla p_2^{n+1} = \frac{1}{\Delta t^{n+1}} (\nabla \cdot \mathbf{u}^* - \nabla \cdot \mathbf{u}^{n+1}),$$

$$\nabla^2 p_2^{n+1} - \frac{1}{\rho^{n+1}} \nabla \rho^{n+1} \cdot \nabla p_2^{n+1} = \frac{\rho^{n+1}}{\Delta t^{n+1}} (\nabla \cdot \mathbf{u}^* - \nabla \cdot \mathbf{u}^{n+1}). \quad (39)$$

Using the vector calculus identity  $\rho \nabla \cdot \mathbf{u} = \nabla \cdot (\rho \mathbf{u}) - \mathbf{u} \cdot \nabla \rho$ , we finally rewrite Eq. (39) as:

$$\nabla^2 p_2^{n+1} = \frac{1}{\Delta t^{n+1}} [\nabla \cdot (\rho^{n+1} \mathbf{u}^*) - \rho^{n+1} \nabla \cdot \mathbf{u}^{n+1} - \mathbf{u}^{n+1} \cdot \nabla \rho^{n+1}]$$

$$+ \frac{1}{\Delta t^{n+1}} \left[ \underbrace{\left( \mathbf{u}^{n+1} - \mathbf{u}^* + \frac{\Delta t^{n+1}}{\rho^{n+1}} \nabla p_2^{n+1} \right) \cdot \nabla \rho^{n+1}}_{= 0 \text{ due to Eq. (33)}} \right]. \quad (40)$$

As  $p_2^{n+1}$  and  $\mathbf{u}^{n+1}$  are both unknown, we solve Eq. (40) together with Eq. (33) by an iterative loop, as reported in the pseudocode Algorithm 1. Two interesting features emerge when using this method. First, the constant-coefficient Poisson Eq. (40) is an equivalent and exact formulation of its variable counterpart (32), derived using the correction step (33). This represents a major difference with respect to the previous two methods, Eq. (36) and (38), which are only a consistent but not

exact recast of Eq. (32). Second, this method allows us to define and control the residual of the iterative procedure on the basis of the velocity divergence, which represents the constraint to be imposed on the flow field. These two advantages come at the cost of performing a correction step for each iteration of the loop. Nevertheless, the additional computational cost is more than compensated by the lower numbers of iterations required to achieve convergence as the solution of the Poisson equation is often the most expensive part in standard two-fluid solvers. As we will show in the result section, this approach requires a significantly lower number of iterations.

The proposed methodology is outlined in the pseudocode Algorithm 1 where the iterations are performed until  $\varepsilon \leq \varepsilon_t$ , is satisfied. The residual  $\varepsilon$  is computed with a summation over the whole computational domain whereas the threshold value  $\varepsilon_t$  is chosen considering the trade-off between the number of iterations required to achieve convergence and the minimization of the residual error. Unless otherwise stated, in the present work,  $\varepsilon_t$  equal to  $10^{-14}$  has been set in order to impose the divergence constraint on the final velocity field,  $\mathbf{u}^{n+1}$ , with machine precision. It should be also noted that the first two terms of Eq. (40) do not vary over the solution cycle and can be pre-computed just before the iterative procedure to reduce the execution time, whereas the last term,  $\mathbf{u}^s \cdot \nabla \rho^{n+1}$  needs to be updated at every iteration of the pressure-correction loop.

Note that an additional possibility to efficiently solve (32) in one single iteration would be to employ the approach described in Method I and instead of solving iteratively Eq. (36) and (37), set  $p_2^{s+1} = p_2^n$  and compute  $p_2^s$  with a linear extrapolation, i.e.,  $p_2^s = 2p_2^n - p_2^{n-1}$ , as already employed for incompressible two-phase simulations [65]. As shown in the result Section 4.2, we obtain identical results when the ratio between the initial liquid and gas temperature is moderate, while we observe deviations from the exact solution for higher temperature ratios. As also observed in [56], we attribute this error to the approximation of  $p_2^s$  with a linear extrapolation, which becomes inaccurate as the temperature gradients between the phases increase.

Before proceeding to the discussion of the validation cases, it is worth mentioning that the proposed mathematical and numerical framework can be naturally extended to any interface capturing and tracking method consistent with the sharp-interface definition of the phase indicator function as in Eq. (1), e.g. Volume-of-Fluid, Level-set and Front-Tracking methods. Furthermore, as also in different implementations of the diffuse interface approach (e.g. phase field models based on the Cahn-Hilliard and Cahn-Allen equations) the numerical procedure is typically based on the solution of a variable coefficient Poisson equation, we believe that the methodology proposed here can be helpful also to generalize the phase field theory in a low-Mach number framework.

---

**Algorithm 1** Solution of the pressure equation with Method III.

---

```

1:  $s = 0$ ,
2:  $\mathbf{u}^s = \mathbf{u}^*$ ,
3:  $\varepsilon = a\varepsilon_t$  with  $a > 1$ .
4: while  $\varepsilon > \varepsilon_t$  do
5:    $s = s + 1$ ,
6:    $\nabla^2 p_2^{s+1} = \frac{1}{\Delta t^{n+1}} [\nabla \cdot (\rho^{n+1} \mathbf{u}^*) - \rho^{n+1} \nabla \cdot \mathbf{u}^{n+1} - \mathbf{u}^s \cdot \nabla \rho^{n+1}]$ ,
7:    $\mathbf{u}^{s+1} = \mathbf{u}^* - \frac{\Delta t^{n+1}}{\rho^{n+1}} \nabla p_2^{s+1}$ ,
8:    $\varepsilon = \sum_{i=1}^{N_x} \sum_{j=1}^{N_y} \sum_{k=1}^{N_z} ||\nabla \cdot \mathbf{u}_{i,j,k}^{s+1} - \nabla \cdot \mathbf{u}_{i,j,k}^{n+1}||$ .
9: end while
10:  $p_2^{n+1} = p_2^{s+1}$ ,
11:  $\mathbf{u}^{n+1} = \mathbf{u}^{s+1}$ .

```

---

**3.4. Time step restriction**

The time step  $\Delta t^{n+1}$  is estimated from the stability constraints of the overall system:

$$\Delta t^{n+1} = C_{\Delta t} \min(\Delta t_c, \Delta t_\sigma, \Delta t_\mu, \Delta t_e)^{n+1}, \quad (41)$$

where  $\Delta t_c$ ,  $\Delta t_\sigma$ ,  $\Delta t_\mu$  and  $\Delta t_e$  are the maximum allowable time steps due to convection, surface tension, momentum diffusion and thermal energy diffusion, respectively. These can be determined as suggested in reference [66]:

$$\Delta t_c = \left( \frac{|u_{x,\max}|}{\Delta x} + \frac{|u_{y,\max}|}{\Delta y} + \frac{|u_{z,\max}|}{\Delta z} \right)^{-1},$$

$$\Delta t_\mu = \left[ \max \left( \frac{\mu_g}{\tilde{\rho}_g^m}, \frac{\mu_l}{\rho_l} \right) \left( \frac{2}{\Delta x^2} + \frac{2}{\Delta y^2} + \frac{2}{\Delta z^2} \right) \right]^{-1},$$

$$\Delta t_\sigma = \sqrt{\frac{(\bar{\rho}_g^m + \rho_l) \min(\Delta x, \Delta y, \Delta z)^3}{4\pi\sigma}},$$

$$\Delta t_e = \left[ \max\left(\frac{k_g}{\bar{\rho}_g^m}, \frac{k_l}{\rho_l c_{p,l}}\right) \left(\frac{2}{\Delta x^2} + \frac{2}{\Delta y^2} + \frac{2}{\Delta z^2}\right) \right]^{-1}, \quad (42)$$

where  $|u_{i,\max}|$  is an estimate of the maximum value of the  $i$ th component of the flow velocity and  $\bar{\rho}_g^m$  is the minimum gas density computed over the computational domain to account for the compressible effects. For the cases presented here,  $C_{\Delta t} = 0.25$  was found sufficient for a stable and accurate time integration and, unless otherwise stated, this value has been employed for the validation cases.

#### 4. Validation and testing

In order to validate and test the proposed numerical approach, five different flow configurations are considered, denoted *C1a*, *C1b*, *C2*, *C3*, *C4* and *C5*. The first two simulations, *C1a* and *C1b*, reproduce the two-dimensional flow originating in a fluid system made of alternating gaseous and liquid bands at different initial densities and temperatures confined in a periodic, free-slip channel. We believe that these test cases are particularly significant to highlight the capabilities of the proposed numerical methodology. The third simulation, *C2*, reproduces a two-dimensional gas bubble rising in an incompressible liquid medium and is used as a quantitative validation against a reference case from archival literature. We select this test case in order to perform the comparison among the different methods analyzed in Section 3.3. The previous setup is also used to study the flow in the presence of three rising bubbles, case *C3*. The fourth test case, *C4*, reproduces a time-evolving, plane mixing layer originating between two streams at different temperatures and opposite velocities. One of the streams is assumed to be compressible, the other being incompressible. The effect of the temperature gradients on the temporal evolution of the mixing layer is fully described by means of the low-Mach number asymptotic approach, taking into consideration thermal diffusion as well as density gradients in the flow. The final test case, *C5*, considers a three-dimensional turbulent bubble-laden flow in a vertical channel, where the flow is heated and cooled by the channel walls. Two simulations are carried out: one where the gas phase is incompressible and one where it is compressible. Differences in the bubble distribution inside the domain are documented below.

##### 4.1. Expansion of gas bands enclosed by an incompressible medium

The test case *C1* reproduces the two-dimensional, isochoric (*C1a*) and isobaric (*C1b*) transformation of a compressible gas band enclosed within an incompressible liquid medium. All the quantities are provided in the non-dimensional frame, the reference values and the simulation parameter being reported in Table 1. The domain is rectangular and extends, in non-dimensional units, for  $L_x/\tilde{L} = 4$  and  $L_y/\tilde{L} = 0.5$ ,  $\tilde{L}$  being the reference length scale.

The domain is discretized using  $N_x \times N_y = 128 \times 16$  nodes. Free-slip boundary conditions are applied to the lower and upper edges of the computational domain while an adiabatic, zero-gradient boundary condition is prescribed to the temperature equation. A periodic boundary condition is applied along the  $x$  direction. The isochoric case, *C1a*, considers a rectangular gas band of width  $b/\tilde{L} = 1$  that splits the domain into two parts filled by an incompressible liquid. The band is initially centred around the axial position  $x_c/\tilde{L} = 3$  and extends over the whole domain in the  $y$  direction. The geometrical configuration of the problem is provided in Fig. 1(a). The ratio of the gas to the liquid temperature is initially fixed to  $(T_g/T_l)_i = 5/6$ . The initial temperature and density fields are uniform over each band, the only discontinuities being located on the liquid-gas interface. Fig. 1 provides also the temporal evolution of the thermodynamic pressure for the gas phase together with a plot of the density, temperature and volume fraction as a function of the axial position,  $x/\tilde{L}$ , at four different time instants. As a result of the initial temperature gradient, a heat flux develops from the liquid region towards the gas band. The temperature of the latter increases as shown in Fig. 1(b), while its density decreases as can be observed in Fig. 1(c). It should be noted that, the prescribed boundary conditions do not allow any volume change of the gas region. Hence, the transformation is isochoric, the volume fraction field remains unchanged and the gas band does not change the position of its centroid neither its boundaries during the transient as can be seen in Fig. 1(d). In these conditions, the energy transfer to the gas band enforces the thermodynamic pressure to progressively increase until a uniform temperature field is established over the entire domain. At this point, the thermodynamic pressure settles to a constant value.

In the second test case, *C1b*, we address the simulation of the isobaric contraction and expansion of two separated gaseous bands enclosed within an incompressible liquid medium. The domain size, discretization and boundary conditions are unchanged and similarly for the fluid parameters which are provided in Table 1. The initial configuration of the fluid system is provided in Fig. 2(a). Initially, the two rectangular gas bands extend over a length  $b/\tilde{L} = 1$  along the  $x$  direction, separated by an incompressible liquid. The left-side band centroid is located at the axial position  $x_{c1}/\tilde{L} = 1$  while the right-side band is centered around  $x_{c2}/\tilde{L} = 3$ . The ratio between the initial gas and liquid temperatures is set to  $(T_{g,1}/T_l)_i = 4/3$  for the left-side band and to  $(T_{g,2}/T_l)_i = 2/3$  for the right-side region. The initial temperature and density fields are uniform over each of the five different regions composing the fluid system. The initial thermodynamic pressure is the same in the two gaseous regions. Fig. 2(c) and (d) provide the temperature and the density fields as a function of  $x/\tilde{L}$  at four different time instants. The colder, right-side, band absorbs energy from the surrounding liquid medium while the hotter band on the left-side releases energy to the surrounding fluid. Hence, we observe the expansion of the colder gas band, simultaneously with the equivalent compression of the hotter gas, as shown in Fig. 2(e) providing the volume fraction as a function of  $x/\tilde{L}$  at four different time instants. The vol-

**Table 1**

Physical dimensionless parameters of the fluids for cases *C1a*, *C1b*, *C2*, *C3*, *C4* and *C5*: the Reynolds number,  $Re$ , the Weber number,  $We$ , the Froude number,  $Fr$ , the Prandtl number  $Pr$ , the density ratio  $\rho_l/\bar{\rho}_{g,r}$ , viscosity ratio,  $\mu_l/\bar{\mu}_{g,r}$ , thermal conductivity ratio,  $k_l/\bar{k}_{g,r}$ , specific heat capacity ratio at constant pressure,  $c_{p,l}/\bar{c}_{p,g}$ . The subscript, "l", refers to the liquid phase and the subscript "g, r" to the reference value in the gas phase. Unless otherwise stated, the dimensionless group  $\Pi_p$  is set equal to 1 for all the case.

	Re	We	Fr	Pr	$\rho_l/\bar{\rho}_{g,r}$	$\mu_l/\bar{\mu}_{g,r}$	$c_{p,l}/\bar{c}_{p,r}$	$k_l/\bar{k}_{g,r}$
Section 4.1	1	$\infty$	$\infty$	1	varied	20	4.186	20
Section 4.2	35	1	1	0.7	varied	10	4.186	20
Section 4.3	125	0.125	1	0.7	10	10	4.186	20
Section 4.4	200	$\infty$	$\infty$	8.92	5	20	4.186	20
Section 4.5	4000	889	4	1.49	10	1	4	1

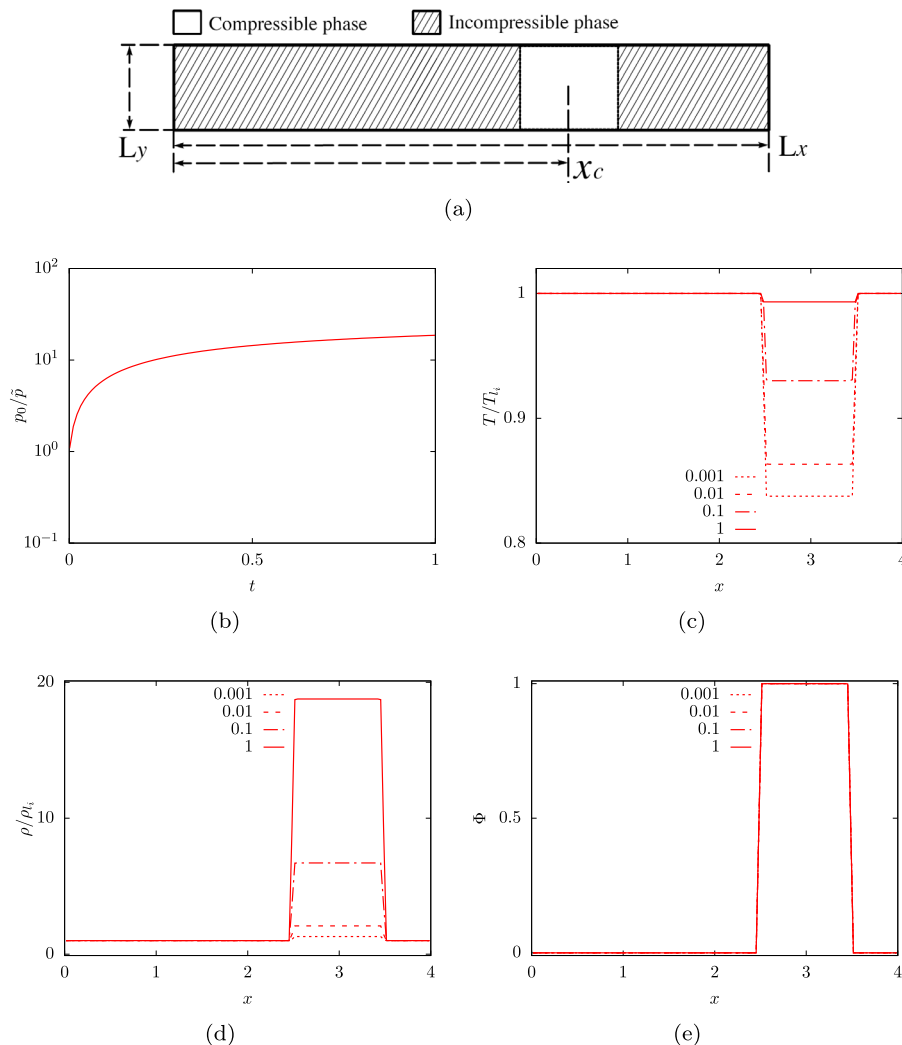


**Fig. 1.** a) Schematic of the computational domain and initial conditions for the test case *C1a*. b) Non-dimensional thermodynamic pressure,  $p_0/\bar{p}$ , in the gas regions as a function of the non-dimensional time,  $t/\bar{t}$ . c) Non-dimensional temperature,  $T/T_{i,j}$ , computed on the middle-line of the domain as a function of non-dimensional coordinate  $x/\bar{L}$ . d) Non-dimensional density,  $\rho/\rho_{i,j}$ , computed on the middle-line as a function of  $x/\bar{L}$ . e) Volume fraction,  $\Phi$ , computed on the middle-line as a function of  $x/\bar{L}$ . The temperature, density and volume fraction curves are provided for four different time instants,  $t/\bar{t} = 0.001$ ,  $t/\bar{t} = 0.01$ ,  $t/\bar{t} = 0.1$  and  $t/\bar{t} = 1$ ,  $\bar{t}$  being the reference time scale.

ume of the liquid region included between the two gaseous bands cannot change; however, due to the periodic boundary condition along the  $x$  direction, the liquid fluid can move from the right to left side of the domain. The two bands do not change the position of their center of mass during the expansion and contraction. Since in this case the volume of each band can vary freely, the transformation is isobaric as can be seen in Fig. 2(b). Even if we cannot provide an analytical solution for the cases *C1a* and *C1b*, we believe that their numerical outcomes clearly show the capability of the method to account for heat transfer, density and temperature gradients as well as for compressibility effects in both isobaric and isochoric conditions in the low-Mach number regime.

The outcome of a spatial convergence study for test case *C1b* is provided in Fig. 3. The figure displays the volume fraction,  $\Phi$ , as a function of  $x/\bar{L}$  at time  $t/\bar{t} = 15$ , computed using four different resolutions. These grid spacing are obtained scaling the base computational grid ( $128 \times 16$  nodes) by the factors 0.5, 1.0, 2.0 and 3.0, corresponding to  $64 \times 8$ ,  $128 \times 16$ ,  $256 \times 32$  and  $384 \times 48$  nodes along the  $x$  and  $y$  directions. Only minor differences can be observed between the results obtained with the highest and lowest grid resolutions. Hence, the base computational grid,  $128 \times 16$ , is suitable for both test cases *C1a* and *C1b*.

#### 4.2. Rising bubble

The test case *C2* addresses the simulation of a two-dimensional rising bubble flow. A circular gaseous bubble of initial density  $\rho_g$  and temperature  $T_g$  is immersed in a liquid fluid with a higher, constant density,  $\rho_l$ , and temperature,  $T_l$ . Both the temperature and the density fields are initially uniform within the bubble and the liquid phase while a discontinuity exists across the interface. The initial configuration is displayed in Fig. 4. The rectangular computational domain extends, in non-dimensional units, for  $L_x/\bar{L} \times L_y/\bar{L} = 1 \times 2$ . The domain is discretized using  $N_x \times N_y = 128 \times 256$  nodes. The initial bubble diameter is  $d_i/\bar{L} = 0.5$  while the bubble center is initially located at  $\mathbf{X}_{c,i}/\bar{L} = (0.5, 0.5)$ . A no-slip and no-penetration boundary condition is prescribed to the momentum equation along the lower and the upper edges of the domain while a zero-gradient boundary condition is applied to the temperature equation. A periodic boundary condition is prescribed along the  $x$  direction. The physical parameters of the fluids are provided in Table 1. We report the results of five different test cases with different initial temperature ratios,  $(T_l/T_g)_i = 1, 1.2, 1.5, 2$  and  $3$ , and corresponding density ratios,  $(\rho_l/\rho_g)_i = 10, 8.33, 6.67, 5$  and  $3.33$ . We use as output quantities the center of mass of the bubble and

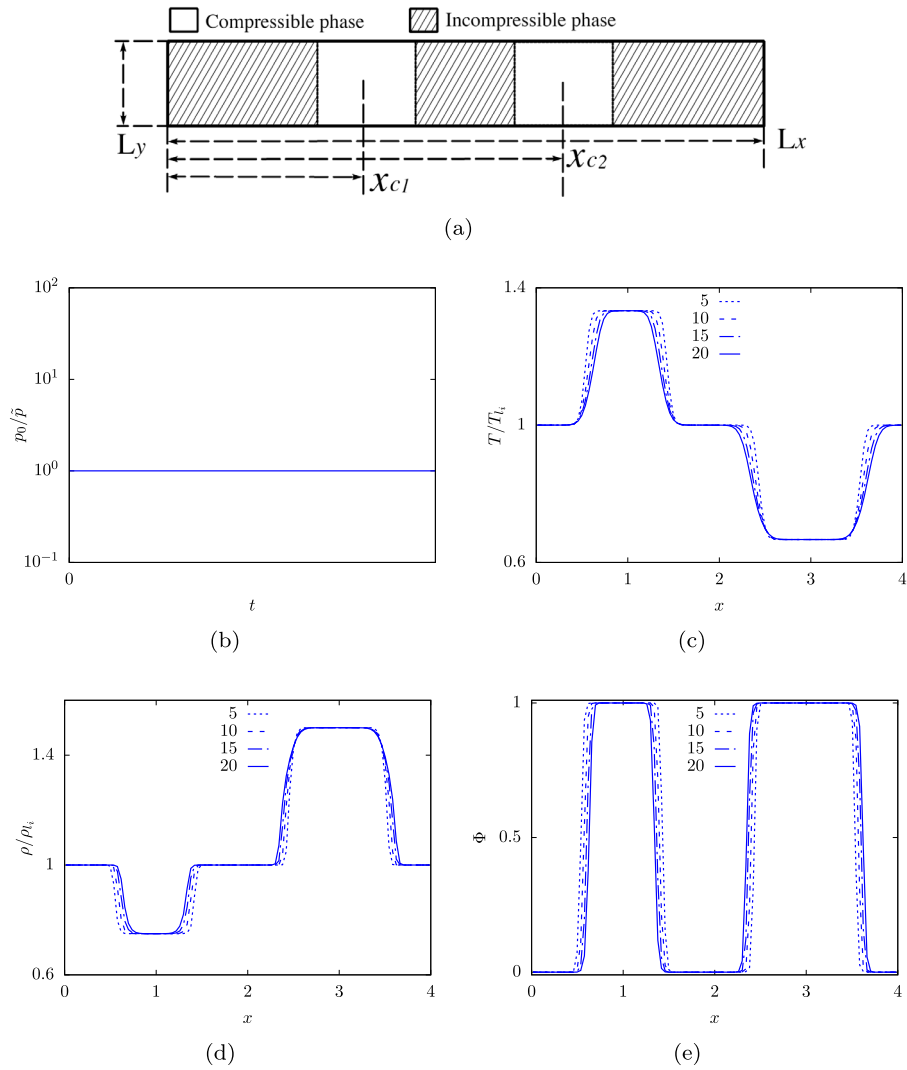


**Fig. 2.** a) Schematic of the computational domain and initial conditions for the test case *C1b*. b) Thermodynamic pressure,  $p_0/\bar{p}$ , in the gas regions as a function of the non-dimensional time,  $t/\bar{t}$ . c) Temperature,  $T/T_{i1}$ , as a function of  $x/\bar{L}$ . d) Density,  $\rho/\rho_{i1}$ , as a function of  $x/\bar{L}$ . e) Volume fraction,  $\Phi$ , as a function of  $x/\bar{L}$ . The temperature, density and volume fraction are provided for four different time instants,  $t/\bar{t} = 5$ ,  $t/\bar{t} = 10$ ,  $t/\bar{t} = 15$  and  $t/\bar{t} = 20$ .

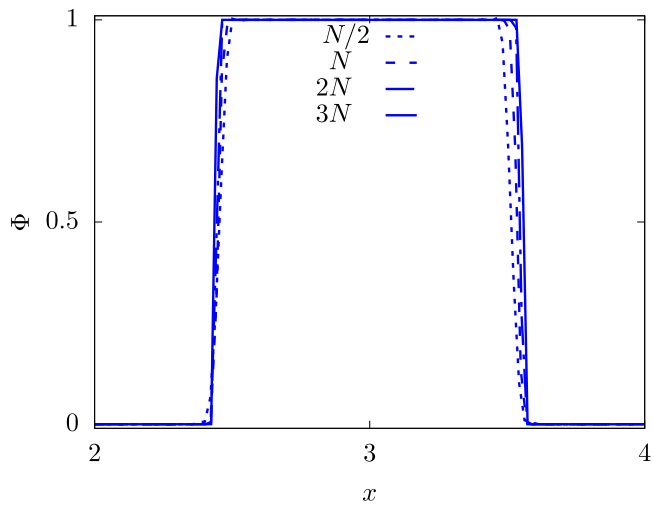


**Fig. 3.** Volume fraction,  $\Phi$ , as a function of  $x/\bar{L}$ , evaluated at time  $t/\bar{t} = 15$ , computed using four different grid resolutions:  $N/2$ ,  $N$ ,  $2N$  and  $3N$ , where  $N$  refers generically to the number of grid nodes per direction ( $x$  and  $y$ ).

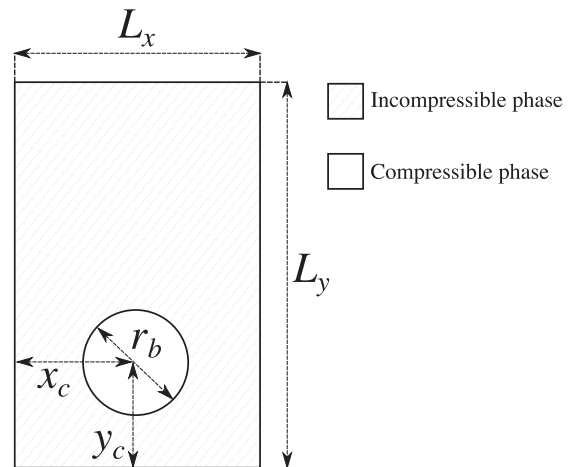


**Fig. 4.** Schematic of the computational domain and initial configuration used for the rising bubble simulation.

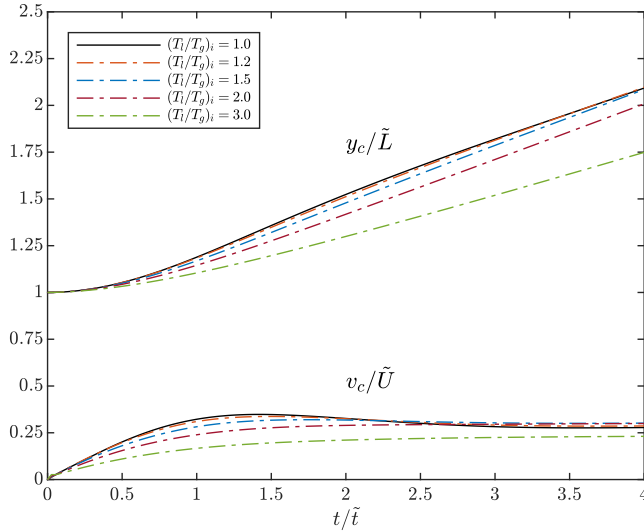


**Fig. 5.** Rising bubble: vertical position of the bubble centroid,  $y_c(t)/\tilde{L}$ , and vertical component of the bubble rising velocity,  $v_c(t)/\tilde{U}$ , versus time,  $t/\tilde{t}$  for a density ratio in the incompressible reference case equal to 10.

the bubble rising velocity. The bubble centroid is defined as

$$\mathbf{X}_c = (x_c, y_c) = \frac{\int_{V_g} \rho_g \mathbf{x} dV_g}{\int_{V_g} \rho_g dV_g}. \quad (43)$$

In a similar fashion, the bubble rising velocity is defined as the mean velocity with which the gas phase is moving,

$$\mathbf{U}_c = (u_c, v_c) = \frac{\int_{V_g} \rho_g \mathbf{u} dV_g}{\int_{V_g} \rho_g dV_g}. \quad (44)$$

In both expressions, the gas volume  $V_g$  is approximated using Eq. (30). Fig. 5 displays the vertical position of the bubble centroid,  $y_c(t)/\tilde{L}$ , and the vertical component of the bubble rising velocity,  $v_c(t)/\tilde{U}$ , versus time,  $t/\tilde{t}$ , for each of the initial temperature ratios given above. In the isothermal case the initial temperature field is uniform over the entire domain,  $(T_l/T_g)_i = 1$ , and the density ratio is set to  $(\rho_l/\rho_g)_i = 10$ . The results of the present simulation are compared with that obtained by Hysing et al. [67]. As the density ratio,  $(\rho_l/\rho_g)_i$ , is decreased, the rising velocity of the bubble is initially lower than in the isothermal case due to the lower buoyancy force exerted by the liquid on the gas bubble. Nonetheless, the thermal diffusion reduces progressively the temperature gradient between the two phases. The bubble heats-up and the density ratio,  $\rho_l/\rho_g$ , increases. As a result, after an initial transient, the terminal bubble rising velocity tends to settle to the same regime velocity as that of the isothermal case, independently of the initial density ratio,  $(\rho_l/\rho_g)_i$ . Clearly, the initial differences in the rising velocities lead to an offset in the position of the bubble centroid.

This case is then repeated at a density ratio equal to 50 (in the incompressible cases) and for two different initial temperature ratios,  $(T_g/T_l)_i = 1.0$  and 3.0, while keeping fixed the other dimensionless parameters, see Table 1. The results, reported in Fig. 6, are qualitatively similar to those at lower density ratio (same rising velocity and offset of the bubble centroid), but given the larger initial density difference, the change of the buoyancy forces due to compressibility effects is less.

As mentioned in Section 2.2, an alternative and efficient way to solve the Poisson equation in one iteration is to employ the time-pressure splitting [65]. Here, we compare this with the iterative

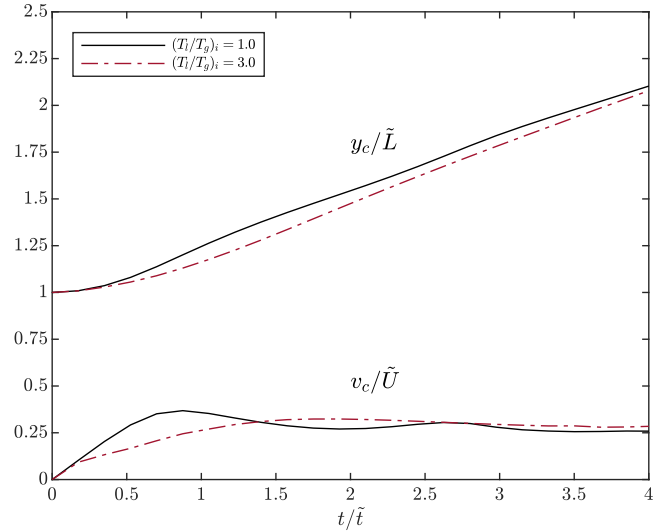


**Fig. 6.** Rising bubble: vertical position of the bubble centroid,  $y_c(t)/\tilde{L}$ , and vertical component of the bubble rising velocity,  $v_c(t)/\tilde{U}$ , versus time,  $t/\tilde{t}$  for a density ratio in the incompressible reference case equal to 50.

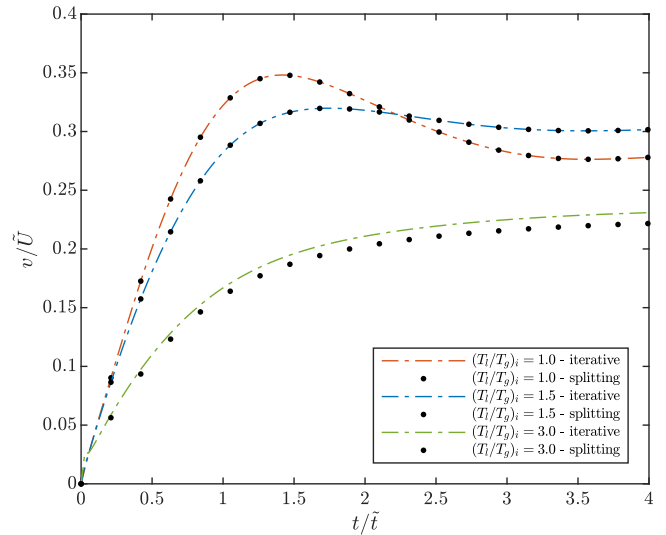


**Fig. 7.** Comparison of the proposed iterative method (Method 3) and the time-splitting approach to solve the Poisson equation. The density ratio of the incompressible reference case is 10 for 3 temperature ratios,  $(T_l/T_g)_i = 1.0 - 1.5 - 3.0$ .

method proposed in the current work for the case of the rising bubble considering three different initial temperature ratios. The results are reported in Fig. 7: for the incompressible case, direct and iterative solvers yield to the same numerical solution. This is confirmed also for intermediate  $(T_l/T_g)_i$ , while we observe deviations in the rising velocity  $v/\tilde{U}$  for the case  $(T_l/T_g)_i = 3$ . As mentioned in Section 2.2, we attribute this deviation to the approximation of  $p_2^s$  in the time-splitting approach, which becomes less and less accurate as thermal gradients become sharper, independently of the density ratio. In fact, when we increase  $(T_l/T_g)_i$ , the velocity divergence increases due to higher thermal gradients at the interface, determining steep time-variation of the thermodynamic pressure  $p_{th}$ . As already discussed in [56], this results in a poor calculation of  $\rho_0$  in Eqs. (36), (37) and ultimately leads to inaccurate results.

To conclude the analysis of this test case, we compare the three methods presented in Section 3.3 in terms of number of iterations needed to solve the Poisson equation. Since the three methods re-

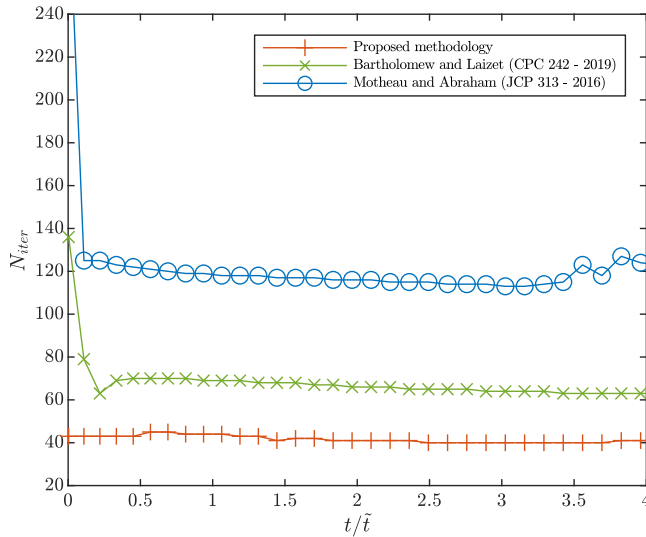


**Fig. 8.** Number of iterations required to solve the pressure Poisson equation for the rising bubble test case as a function of time  $t/\tilde{t}$ . The data are obtained using the methods by Bartholomew and Laizet [64], Motheau and Abraham [56] and the present method. We consider the case  $(T_l/T_g)_i = 1.2$  (e.g.,  $(\rho_l/\rho_g)_i = 8.33$ ). The reference time scale  $\tilde{t} = \sqrt{d_0/g}$ .

quire different tolerances to satisfy the divergence constraint with the same accuracy, we set  $\varepsilon_t = 10^{-8}$  for *Method 1* and  $\varepsilon = 10^{-11}$  for *Method 2* and *3* for a fair comparison. Using these different thresholds,  $\varepsilon_t$ , leads to similar values of the residual (below  $10^{-14}$ ), computed as the difference between the velocity divergence and its constraint according to Eq. (35). For what concerns *Method 3*, and only for this case, we compute the residual  $\varepsilon$  on the pressure between two consecutive iterations and not on the velocity divergence. Once again, this choice is motivated by a fair comparison with the other two methods. Indeed, for *Method 1* and *Method 2*, the residual based on the pressure  $p_2$  is the only possible choice being the correction step performed only at the end. The results provided in Fig. 8 clearly show that the current approach, *Method 3*, requires a number of iterations between 1.5 and 3 times lower than that of *Method 1* and *Method 2* to achieve a full convergence. As mentioned above, we attribute this faster convergence to the exact way we recast the variable-coefficient Poisson equation into a constant-coefficient problem using directly the correction step.

### 4.3. Multiple rising bubbles

In this section, we consider the same configuration adopted in the previous test case to study the flow in the presence of three compressible bubbles, rising in an incompressible liquid. The bubbles have the same initial diameter,  $d_i$  and are initially at rest in a rectangular domain of dimensions  $L_x/\tilde{L} \times L_y/\tilde{L} = 7.2 \times 12.8$ , being the reference length  $\tilde{L} = d_i$ . The initial position of the bubble centroids are set to  $(\mathbf{X}_{c,1}/\tilde{L})_i = (1.8, 1.25)$  for *Bubble n.1*,  $(\mathbf{X}_{c,2}/\tilde{L})_i = (3.6, 1.25)$  for *Bubble n.2* and  $(\mathbf{X}_{c,3}/\tilde{L})_i = (5.4, 1.25)$  for *Bubble n.3*. The initial temperature and density of the liquid phase are  $T_l$  and  $\rho_l$ , respectively. In order to highlight the compressibility effects, the three bubbles are initialized at three different temperatures,  $(T_{g,1}/T_l)_i = 1.5$ ,  $(T_{g,2}/T_l)_i = 1.0$  and  $(T_{g,3}/T_l)_i = 0.75$  as reported on the left panel of Fig. 9. In order to avoid bubble coalescence and merging, we consider a limited Weber number  $We = \rho_{g,0}^m \tilde{U}^2 d_0 / \tilde{\sigma} = 0.125$  and we set the Reynolds number  $Re = \rho_{g,0}^m \tilde{U} d_0 / \mu_g = 125$ , where  $\tilde{U} = \sqrt{g d_0}$  and  $\rho_{g,0}^m$  is the minimum initial gas density. The Prandtl number  $Pr = \mu_g k_g / c_{p,g}$  is set to 0.7. All the other dimensionless parameters are kept the same as in the previous case and

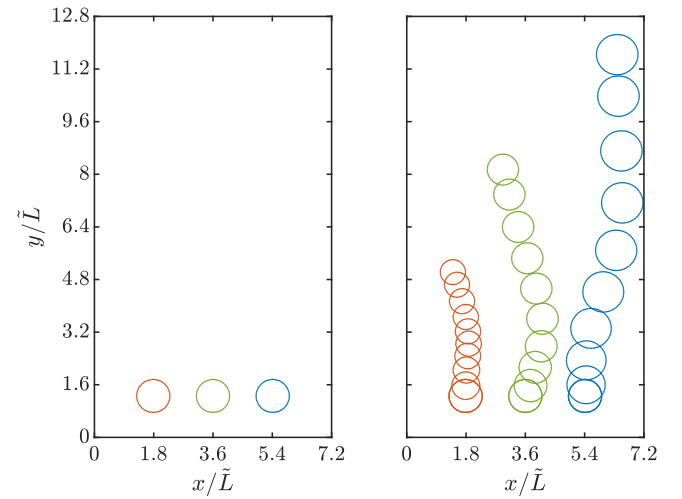


**Fig. 9.** Position of the three rising bubbles at  $t/\tilde{t} = 0$  (left panel) and for  $t/\tilde{t} > 0$  (right panel). The interface position is taken from the grid points where  $\Phi = 0.5$  and the bubble contour are plotted with at the dimensionless physical time  $t/\tilde{t} = \{0, 1.5, 3.0, 4.5, 6.0, 7.5, 9.0, 10.5, 12.0, 13.5\}$ , with the reference time scale being  $\tilde{t} = \sqrt{d_0/g}$ .

are reported in Table 1. Since the system is closed and thermally isolated, once the bubbles start to rise, the heat transfer exchanged among each other and with the liquid medium drives them towards the thermal equilibrium. In detail, *Bubble n.1* starts to cool down, *Bubble n.2* maintains an almost constant average temperature, whereas *Bubble n.3* is heated up. As a result and owing to the variation of the thermodynamic pressure, the first bubble contracts increasing its mean density, the third bubble expands decreasing its mean density, whereas the second one slightly expands mainly due to the variation of the thermodynamic pressure. As shown in Fig. 10, after  $t/\tilde{t} \approx 6$ , being  $\tilde{t} = \sqrt{d_0/g}$ , the thermal equilibrium is globally reached and the mean temperature and density remain approximately constant for the three bubbles.

Fig. 11 provides the mean vertical velocity of the centroid of each bubble. The initial expansion and contraction of the bubbles affects the vertical component of their rising velocities computed as in Eq. (44). In particular, until  $t/\tilde{t} \approx 1.8$ , all the three bubbles move with a comparable vertical velocity. After this initial stage, the third bubble starts to accelerate and arrives first at the top wall, whereas the first one starts to decelerate and moves along the vertical direction at an almost constant speed. On the other hand, the second bubble accelerates towards the top wall, but at a lower rate than the third one. The physical explanation for this behavior relies in the modification induced by the initial expansion and contraction stage of the bubbles, which determines an increase of the buoyancy forces for *Bubble n.3* and a reduction for *Bubble n.1*.

### 4.4. Mixing layer

As a final test case, C4, the numerical simulation of a two-dimensional, temporal mixing layer is addressed. This considered flow configuration develops in the region between two counter-directional flows, one of them being compressible, the other incompressible. The streams move with opposite velocities,  $U_g$  and  $U_l$ . In these conditions, a Kelvin-Helmholtz instability promotes the formation of well-defined coherent vortices in the region separating the two streams. The latter enhance micro-mixing and molecular diffusion promoting the exchange of momentum and energy between the opposite streams. The computational domain consists of a square box of unit size,  $L_x/\tilde{L} \times L_y/\tilde{L} = 1 \times 1$ , discretized

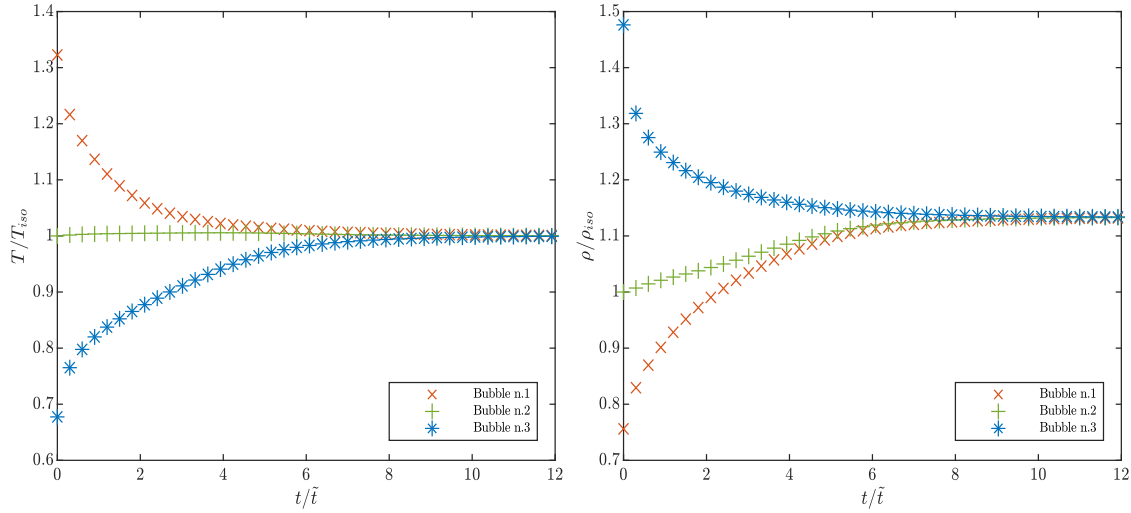


**Fig. 10.** Averaged gas temperature (left panel) and averaged gas density of the three bubbles (right panel) versus non-dimensional time. The initial temperature and density of Bubble n.2 are taken as a reference temperature,  $T_{iso}$ , and density,  $\rho_{iso}$ . The reference time scale is  $\tilde{t} = \sqrt{d_0/|g|}$ .

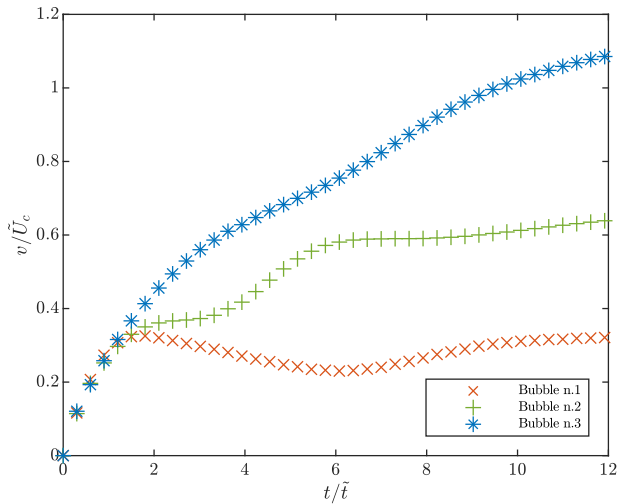


**Fig. 11.** Normalized vertical velocity of the bubbles versus time. The reference velocity scale is  $\bar{U} = \sqrt{|g|d_0}$  while the reference time scale is  $\tilde{t} = \sqrt{d_0/|g|}$ .

using  $N_x \times N_y = 512 \times 512$  nodes. In the lower part of the computational domain,  $0 < y/\tilde{L} \leq 0.5$ , the incompressible flow moves from the right to the left while in the upper part of the domain,  $0.5 < y/\tilde{L} \leq 1$ , the compressible stream moves in the opposite direction. A no-slip boundary condition is prescribed to the momentum equation along the top and bottom sides of the domain while a zero-gradient, adiabatic boundary condition is assigned to the temperature equations along the same boundaries. Periodic boundary conditions are applied to all quantities along the flow direction,  $x$ .

To better characterize the mixing-layer flow, it is worth introducing a length-scale based on the initial vorticity thickness in the mixing layer,  $\delta$ , and a corresponding Reynolds number  $Re_\delta = U_c \delta / \nu_{g,i}$  with  $\nu_{g,i}$  the kinematic viscosity of the gas phase (evaluated at the initial condition) and  $U_c$  a prescribed convective velocity defined as  $U_c = 1/2(U_g - U_l)$ . The initial velocity field is prescribed imposing a pseudo-perturbation on a mean profile according to the following relations [68]:

$$\frac{u(x, y, 0)}{U_c} = \tanh\left(\frac{2\tilde{L}}{\delta}y\right) + \xi_{noise} \frac{\partial \psi}{\partial y}, \quad (45)$$

$$\frac{v(x, y, 0)}{U_c} = -\xi_{noise} \frac{\partial \psi}{\partial x}, \quad (46)$$

$$\psi(x, y) = \exp\left(-\frac{\tilde{L}^2}{\delta^2}y^2\right) [\cos(4\pi x) + 0.03 \sin(10\pi x)], \quad (47)$$

where  $u(x, y, 0)$  and  $v(x, y, 0)$  are the horizontal and vertical components of the initial velocity field. Moreover, the factor  $\xi_{noise} = 10^{-3}$  is chosen to ensure that the velocity perturbations remain a small percentage of the mean velocity, as suggested by the authors in Zayernouri et al. [68]. Prescribing the hyperbolic tangent velocity profile given by Eqs. (45)–(46), the wave-length associated with the initial vortex distribution results to be approximately  $\lambda \simeq 7\delta$  [68,69]. Hence, given the domain size,  $\tilde{L}$  and the desired number of vortices in the periodic domain,  $N$ , the initial vortex thickness is  $\delta/\tilde{L} = 1/(7N)$ . In the present case, the initial vorticity thickness is fixed to  $\delta/\tilde{L} = 1/28$  and  $Re_\delta = 200$ . The non-dimensional viscosity, thermal conductivity and the specific heat capacity ratios are kept equal to unity, while the density ratio based on the initial gas density  $(\rho_l/\rho_g)_i$  is taken equal to 5. Finally, the Prandtl number is set to  $Pr = \mu_g c_{p,g}/k_g = 8.92$  with  $c_{p,g}$  and  $k_g$  being the specific heat capacity and thermal conductivity of the gas phase. The initial temperature field is initialised according to the step-function,

$$T(x, y) = \begin{cases} T_{l,i}, & \text{if } 0 \leq y/\tilde{L} \leq 0.5, \\ T_{g,i}, & \text{if } 0.5 < y/\tilde{L} \leq 1. \end{cases} \quad (48)$$

While keeping fixed the initial liquid temperature  $T_{l,i}$  and the initial density ratio  $(\rho_l/\rho_g)_i$  between the two phases, different initial gas temperatures,  $T_{g,i}$ , gas densities,  $\rho_{g,i}$  and liquid densities  $\rho_{l,i}$ , are prescribed to the compressible and incompressible fluids, as sketched in Fig. 12. A first test case considers the isothermal flow where  $(T_g/T_l)_i = 1$ , whereas three other cases address a temperature ratio equal to 15/16, 5/6 and 3/4, respectively. Fig. 13 provides the temporal evolution of the thermodynamic pressure (uniform over the computational domain), the mean gas and liquid temperature, the mean gas density and the mean kinetic energy for the two phases. The gas and liquid temperatures are computed as integrals over the corresponding domains, whereas the mean kinetic energy is estimated over the compressible and incompressible regions:

$$\bar{T}_g(t) = \frac{1}{M_g} \int_V \rho_g(x, y, z, t) T(x, y, z, t) \Phi(x, y, z, t) dV, \quad (49)$$

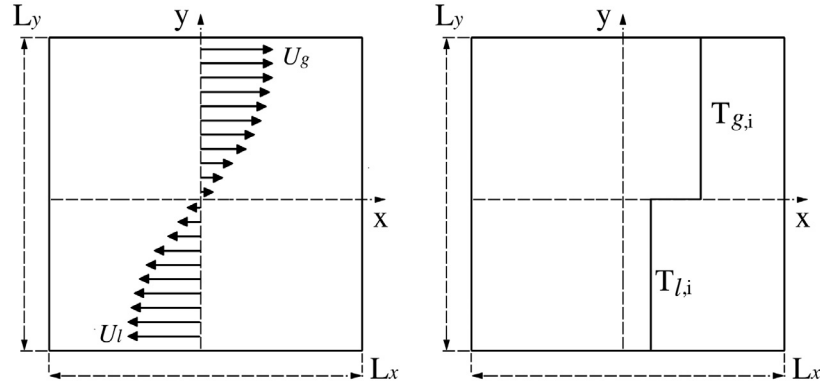


Fig. 12. Sketch of the domain for the temporal mixing-layer simulation showing the initial velocity and temperature fields.

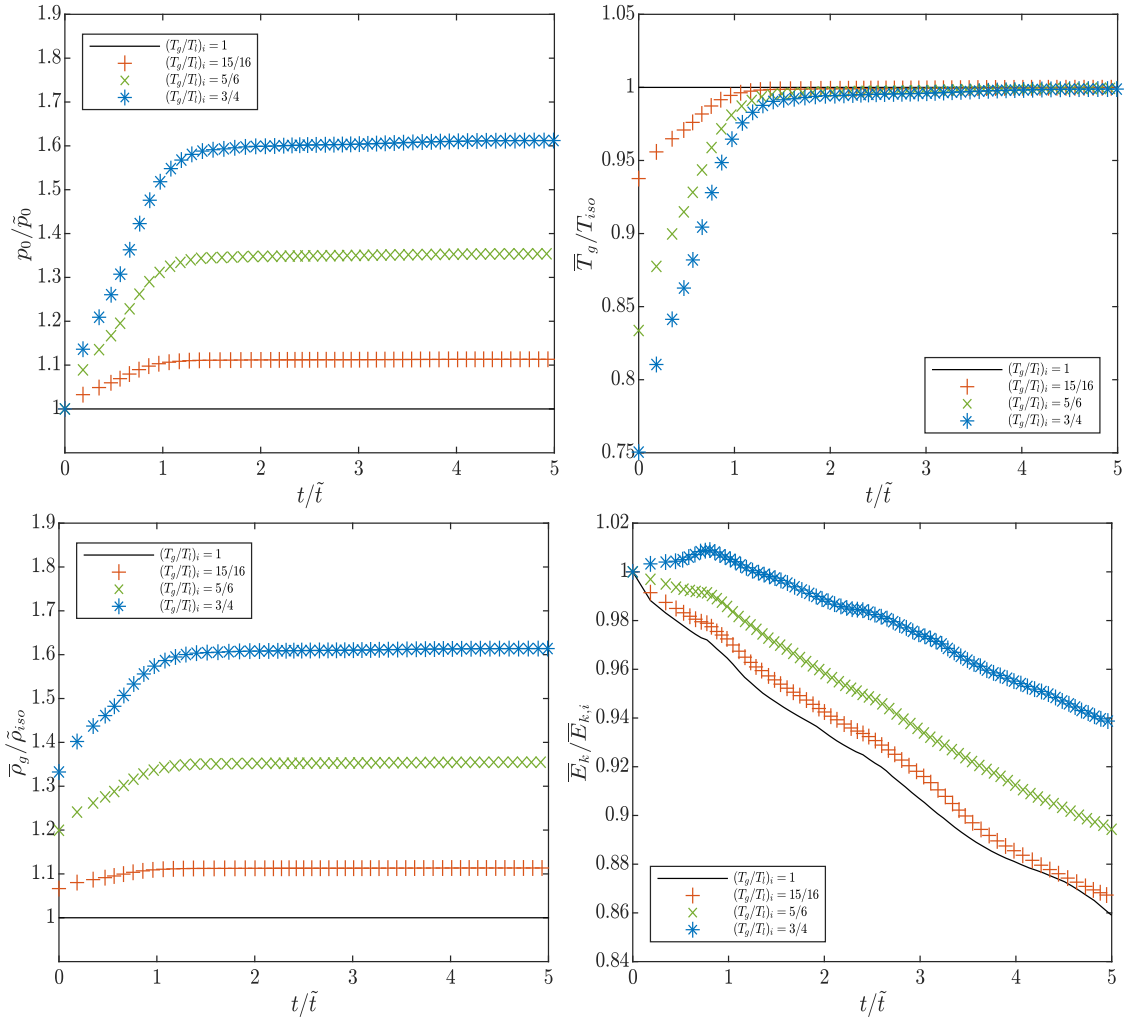


Fig. 13. Temporal evolution of the thermodynamic pressure,  $p_0$ , mean gas temperature,  $\bar{T}_g$ , mean gas density,  $\bar{\rho}_g$  and mean kinetic energy,  $\bar{E}_k$  for the mixing layer at four different temperature ratios,  $(T_g/T_l)_i \in [1.0, 15/16, 5/6, 3/4]$ . All the quantities are non-dimensional using as reference values the values of the isothermal case, except for the mean kinetic energy where we employ the initial value of  $\bar{E}_k$  for each case,  $\bar{E}_{k,i}$ . The reference time-scale  $\tilde{t} = \tilde{L}/\tilde{U}_c$ .

$$\bar{T}_l(t) = \frac{1}{V_l} \int_V T(x, y, z, t) (1 - \Phi(x, y, z, t)) dV, \quad (50)$$

$$\bar{E}_k(t) = \frac{1}{2M_T} \int_V \rho(x, y, z, t) \mathbf{u}(x, y, z, t) \cdot \mathbf{u}(x, y, z, t) dV, \quad (51)$$

where  $M_g$ ,  $V_l$  and  $M_T$  are the mass of the gas, the liquid volume and the total mass of the system, all of them constant during the

simulation. Note that, given the two-dimensional configuration, the numerical calculation of the integrals in Eq. (51) is performed in the two-dimensional  $(x - y)$  plane. Once the mean gas temperature is known, the mean gas density is computed directly from the equation of state whereas the liquid density is constant and equal to  $\rho_l$ ,

$$\bar{\rho}_g(t) = \frac{p_0(t)}{\mathcal{R}\bar{T}_g(t)}, \quad \text{and} \quad \bar{\rho}_l(t) = \rho_l. \quad (52)$$

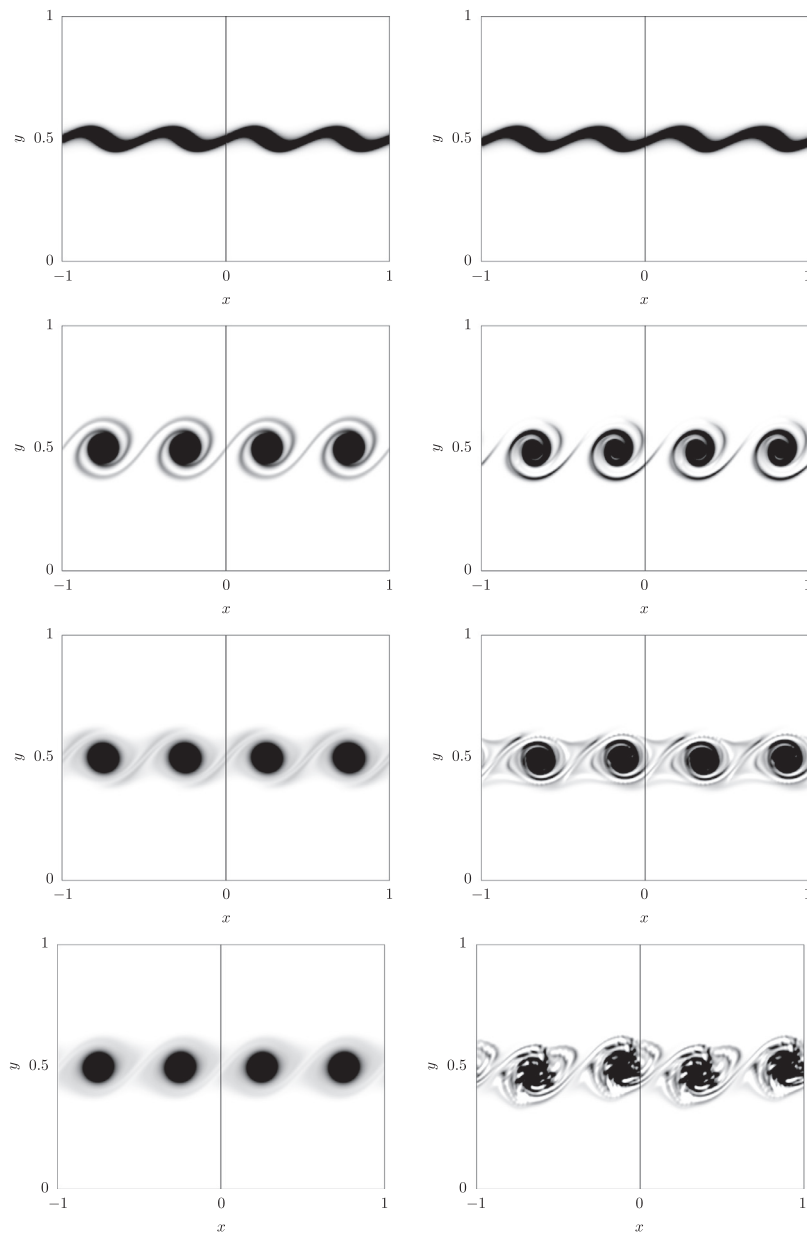


**Fig. 14.** Contour plots of the dimensionless vorticity field  $\omega_z/\bar{\omega}_c$  in the mixing layer for the isothermal case (left panels) and for the  $(T_g/T_l)_i = 3/4$  case (right panel). The contour plots refer to the dimensionless physical time  $t/\tilde{\tau} = 0.01, 0.02, 0.03$  and  $0.04$  in order. The reference time scale is  $\tilde{\tau} = \tilde{L}/U_c$  whereas the vorticity one is  $\bar{\omega}_c = U_c/\tilde{L}$ .

In the isothermal case, the thermodynamic pressure, the mean liquid and gas temperature and the mean gas density do not change over time as shown in Fig. 13. Moreover with the prescribed boundary conditions and in absence of external forces, the mean kinetic energy in the incompressible case (e.g.  $(T_g/T_l)_i = 1$ ) monotonically decreases due to the internal dissipation in the flow. On the other hand, as the temperature ratio is reduced below unity, the turbulent mixing enhances the thermal diffusion between the two fluids thus rapidly reducing the temperature gradients. As a result, the temperature tends to rapidly increase in the colder, compressible stream until a stationary condition is established. As the compressible phase heats up, the thermodynamic pressure,  $p_0$ , and the mean gas density increase. These effects modify the mean kinetic energy balance, that in the compressible cases contains not only the viscous dissipation but also a pressure work term proportional to the gas expansion. This last term modifies the variation of  $E_k/E_{k,i}$  for all the compressible cases and is responsible for the initial increase in the mean kinetic energy observed for the

case  $(T_g/T_l)_i = 0.75$  up to  $t/\tilde{\tau} \approx 1$ ,  $\tilde{\tau} = \tilde{L}/U_c$  being the reference time scale. However, once the temperature gradients become negligible and the thermodynamic pressure has reached a constant value, the compressible effects expire and the mean kinetic energy variation is mainly governed by the viscous dissipation.

Finally, Fig. 14 displays the contour plots of the instantaneous vorticity field at three different physical times for isothermal case and for the initial temperature ratio  $(T_g/T_l)_i = 3/4$ . Despite we limit the analysis at the initial times in order to avoid the loss in resolution induced by the formation of smaller and smaller scales, we observe that, in general, the presence of a temperature gradient enhances the mixing and the growth-rate of the vorticity thickness with respect to the reference, isothermal case.

#### 4.5. Turbulent bubble-laden upflow in a vertical channel

In this final case, C5, the potential of this method to simulate challenging multiphase flows is demonstrated with three-

dimensional simulations of turbulent bubble-laden flows in a differentially heated vertical channel. An incompressible liquid is flowing upwards, against the gravity field, carrying highly-deformable gas bubbles. The bubbles develop a relative upward movement compared to the surrounding liquid due to the density difference of the two fluids. While the liquid density is constant, the gas density is allowed to vary based on the ideal gas law, Eq. (17), resulting in denser bubbles in colder regions and lighter bubbles in hotter regions. This characteristic adds to the complexity of the flow, with the thermal field strongly affecting the behavior of the bubbles in the channel.

To investigate the effects of the thermal field on the flow features, two cases were simulated:

- Case C5-PS: The temperature field is passive and has no effect on the gas properties or the flow in general. The flow is therefore incompressible in both the liquid and the gas phase, and the physical properties are constant within each phase. The mathematical model presented in Section 2.2 is modified by setting the right-hand side of Eqs. (15) and (16) equal to zero, and neglecting Eq. (17). The numerical methodology presented in Section 3.3 is followed by incorporating these modifications.
- Case C5-LM: The temperature field within the gas phase is active, giving rise to low-Mach effects, while the liquid phase is incompressible. The numerical methodology presented in Section 3.3 is followed in full.

A schematic representation of the configuration is shown in Fig. 15. The size of the channel is  $L_x \times L_y \times L_z = \pi \times 2 \times \pi/2$  along the streamwise, wall-normal and spanwise directions respectively. The same configuration was also adopted by Lu and Tryggvason [70,71] to study turbulent incompressible bubble-laden flows. The relevant non-dimensional groups that define the flow are  $Re = 4000$ ,  $We = 889$ ,  $Pr = 4.0$  and  $Fr = 1.49$ , based on  $L_y$  and the liquid properties. In addition, the property ratios are set to  $\rho_l/\tilde{\rho}_{g,r} = 10$ ,  $\mu_l/\tilde{\mu}_{g,r} = 1$ ,  $c_{p,l}/\tilde{c}_{p,g,r} = 4$  and  $k_l/\tilde{k}_{g,r} = 1$ . The volume fraction of the gas phase inside the whole domain is set to 5%. A different temperature value is set on each channel wall, resulting in a temperature difference of  $\Delta T = T_{y=2} - T_{y=0} = 40K$ , while the average temperature between the two walls is set to  $T_0 = 323K$ .

In both simulations, a numerical grid of  $N_x \times N_y \times N_z = 512 \times 512 \times 256$  is adopted, amounting to approximately 67 million grid points. The flow is maintained along the positive  $x$  direction by forcing the flow-rate to a constant value. Periodic boundary conditions are set along the  $x$  and  $z$  directions. The channel walls are

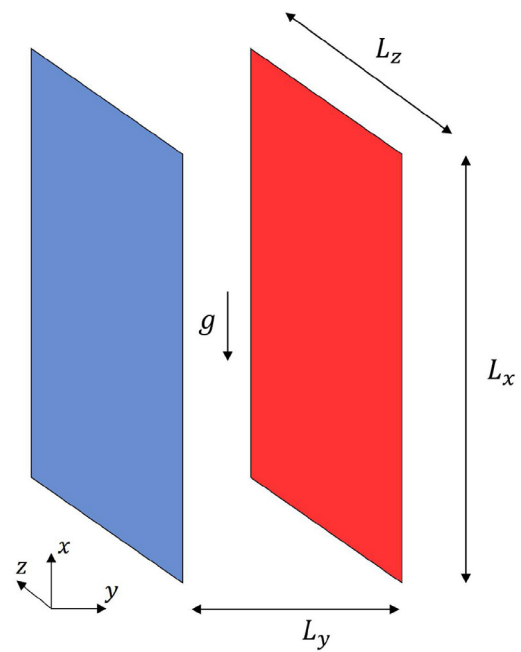


Fig. 15. Schematic representation of the domain used for the simulations of cases C5-PS and C5-LM. The dimensions of the channel are  $L_x \times L_y \times L_z = \pi \times 2 \times \pi/2$ . The flow is directed along the positive  $x$  direction, opposite to the gravitational field, and it is heated and cooled by the red and blue walls. (For interpretation of the references to colour in this figure legend, the reader is referred to the web version of this article.)

considered solid, impermeable and thermally active, therefore a no-slip boundary condition is applied for the velocity field and a Dirichlet boundary condition for the temperature field.

To prepare the initial condition of the turbulent multiphase simulations, a preliminary simulation was ran for the liquid phase only. This flow was initialised with a streamwise vortex pair to achieve a fast transition to turbulence [72]. At this stage, 60 randomly distributed gas bubbles of diameter  $d_b = 0.25$  are introduced inside the domain. The initial bubble distribution is shown in Fig. 16(a), where the bubbles are coloured based on the local values of the stream-wise velocity component. The flow is then allowed to develop for a sufficiently long time. Within this time period, the number of bubbles increased significantly due to exten-

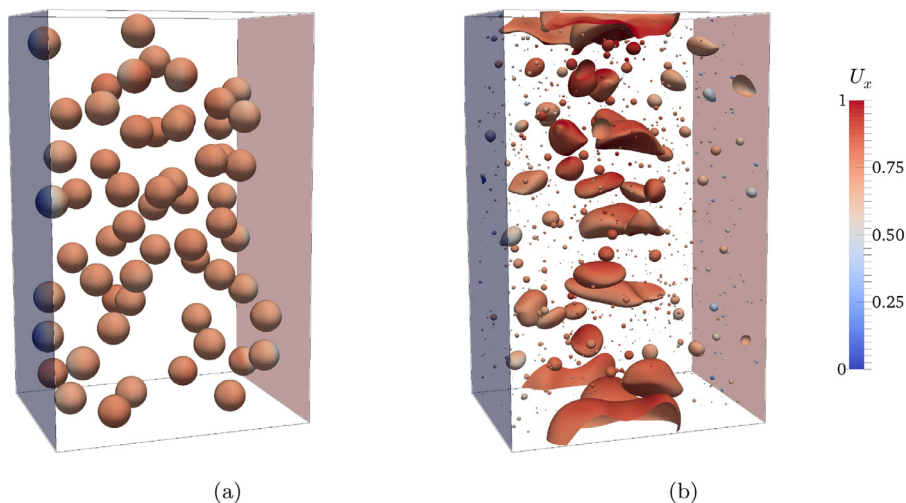
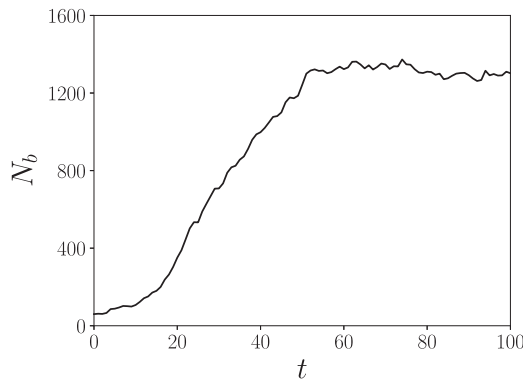


Fig. 16. Distribution of bubbles inside the channel for case C5-LM. (a) Initial condition; (b) statistically steady state. The bubbles are coloured based on the local values of the stream-wise velocity component.



**Fig. 17.** Temporal variation of the number of bubbles in the domain,  $N_b$ , for case C5-PS. Initially 60 bubbles were present inside the domain, and after approximately 60 time units the number of bubbles stabilised at around 1300.

sive break-up, before approximately reaching a plateau. The number of bubbles as a function of time for case C5-PS is shown in Fig. 17, revealing the dynamic balance between break-up and coalescence events after 60 time units. This is an indication that a statistically stationary state has been reached and statistical sampling can start. To ensure that no significant residual transient effects are present to contaminate the statistics, the flow is allowed to develop for additional 60 time units before sampling started. Fig. 16(b) shows the instantaneous bubble distribution inside the domain for case C5-LM, after the flow reached a statistically stationary state.

The averaged gas volume fraction  $\langle \Phi \rangle_{x,z,t}$  and the liquid stream-wise velocity component  $\langle u_x \rangle_{x,z,t}$  are shown as a function of the wall-normal coordinate in Fig. 18, for both C5-PS and C5-LM. As the notation suggests, these quantities are averaged both in time and in wall parallel ( $x - z$ ) planes, along which the flow is assumed periodic. In both cases, the bubbles move away from the walls and migrate towards the interior of the channel. This effect was first observed by Lu and Tryggvason [71] for highly-deformable bubbles that are not affected by the temperature field, such as those considered in C5-PS. The new finding emerging from C5-LM is the shift of the location of the maximum value of  $\langle \Phi \rangle_{x,z,t}$  and  $\langle u_x \rangle_{x,z,t}$  towards the cooled channel wall. At this location, the bubbles are slightly colder and therefore heavier, contributing to the weakening of the buoyancy effect. In addition, the maximum value of  $\langle \Phi \rangle_{x,z,t}$  is smaller for C5-LM, suggesting that the gas phase is more dispersed around the location of the maximum value when compared to C5-PS. Even though the characterisation of the physical mechanism that causes this shift towards the cooled channel wall

is not within the scope of the present study, it is clear that the physically appropriate coupling of the temperature and momentum fields has a big impact on the accurate representation of time-averaged fields, even for this relatively small temperature difference.

### 5. Final remarks

Multiphase, compressible flows are of great interest in a wide range of scientific fields and engineering problems. In this context, we propose a novel approach to the numerical simulation of multiphase, viscous flows where a compressible gas phase and an incompressible liquid mutually interact in the low-Mach number regime. The problem is addressed in the framework of a low-Mach number asymptotic expansion of the compressible formulation of the Navier-Stokes equations. In this limit, acoustics are neglected but large density variations of the gas phase can be accounted for as well as heat transfer between the phases and with the domain boundaries. A Volume of Fluid approach is used to deal with the presence of different phases in the flow as well as for interface tracking. In this specific implementation, the interface reconstruction is based on the MTHINC method [34] while the effect of the surface tension is accounted for using the continuum surface force (CSF) model [45]. The same set of equations is used for both the gas and the liquid phase, the zero-divergence condition being exactly imposed to the latter. To numerically solve this set of equations, we have developed a massive parallel solver, second order accurate both in time and space. The Poisson pressure equation is managed by a FFT-based solver that allows for a numerically efficient and very fast solution procedure. In addition, this choice is suited for code optimization and adaptation of incompressible GPU codes that benefits of FFT-based solvers (e.g. see [73]). The proposed iterative procedure shows to be more efficient in terms of number of iterations than the two approaches available in literature in the context of low-Mach number flows [56,64]. The solver has been build upon a code for incompressible flows which has undergone an extensive validation campaign [46,47]. A detailed and complete description of the theoretical approach is provided, together with information about the numerical techniques employed. Emphasis is given on ensuring the mass conservation of the compressible phase and on correctly imposing the velocity divergence at the pressure-correction step. In addition, we apply the described numerical approach to the simulation of five different flow configurations. The outcomes of two simulations reproducing the two-dimensional expansion and contraction of rectangular gaseous bands enclosed in an incompressible fluid and confined in a free-slip, periodic channel are provided. Next, we address the simulation of two-dimensional rising bubbles. First, we consider a

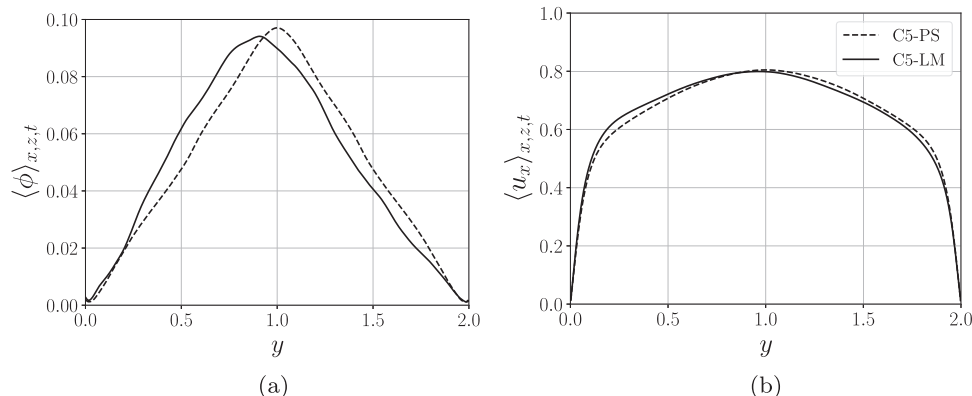


**Fig. 18.** (a) Averaged gas volume fraction  $\langle \Phi \rangle_{x,z,t}$  and (b) liquid stream-wise velocity component  $\langle u_x \rangle_{x,z,t}$  as a function of the wall-normal coordinate. Dashed line, C5-PS; Solid line, C5-LM. In both plots, the location of the maximum value moves towards the colder wall for C5-LM.

single bubble and compare the results of our simulation with the reference data by Hysing et al. [67] using as benchmark quantities the bubble centroid and the bubble rising velocity. Second, we simulate the evolution of three bubbles of the same size but with different initial temperatures. Furthermore, we discuss the outcome of a numerical simulation reproducing a plane, temporal mixing layer and show how the compressibility of the gas phase alters the development of the instability. Finally, the potential of the developed methodology to solve complex three-dimensional flows is demonstrated by simulating a turbulent bubble-laden channel flow, where the two channel walls are heated and cooled. The coupling of the temperature and momentum fields causes the migration of the bubbles closer to the cold wall, revealing the significance of the accurate representation of the buoyancy effects, even for a moderate temperature differences within the domain.

As the proposed mathematical and numerical framework is independent of the capturing/tracking technique used to describe the interface topology, the proposed methodology can be directly extended to other existing numerical codes. We believe that the results presented here demonstrate that it is possible to accurately address the numerical simulation of multiphase, viscous flows in the low-Mach number regime, also when one of the phases can be treated as incompressible. Further extensions of the present methodology may concern the addition of more complex physical phenomena like phase change and complex interfacial thermodynamics, as absorption-desorption processes.

### Declaration of Competing Interest

The authors declare that they have no known competing financial interests or personal relationships that could have appeared to influence the work reported in this paper.

### CRedit authorship contribution statement

**Federico Dalla Barba:** Validation, Writing - review & editing, Writing - original draft. **Nicoló Scapin:** Validation, Writing - review & editing, Writing - original draft. **Andreas D. Demou:** Validation, Writing - review & editing. **Marco E. Rosti:** Conceptualization, Supervision, Writing - review & editing, Writing - original draft. **Francesco Picano:** Conceptualization, Supervision, Writing - review & editing. **Luca Brandt:** Funding acquisition, Conceptualization, Supervision, Writing - review & editing.

### Acknowledgements

N.S., M.E.R. and L.B. acknowledge the support from the Swedish Research Council via the multidisciplinary research environment INTERFACE, Hybrid multiscale modelling of transport phenomena for energy efficient processes and the Grant No. 2016-06119. The computational resources were provided by SNIC (Swedish National Infrastructure for Computing).

### Appendix A. Low Mach number expansion of the Navier-Stokes equations

This appendix provides the derivation of the low-Mach number asymptotic expansion of the governing equations for the compressible gas phase, Eqs. (2)–(5), provided in Section 2.1. All the quantities employed here refer only to the gas phase unless otherwise stated. Under the hypotheses of ideal and calorically perfect gases, the energy equation, Eq. (4), can be re-written in terms of the sensible internal energy or enthalpy only:

$$e = \Delta h_{T_{ref}}^0 + c_v(T - T_{ref}) = \Delta h_{T_{ref}}^0 + c_v T, \quad (A.1)$$

$$h = \Delta h_{T_{ref}}^0 + c_p(T - T_{ref}) = \Delta h_{T_{ref}}^0 + c_p T, \quad (A.2)$$

with  $h = e + p/\rho$  the enthalpy,  $T$  the temperature and  $\Delta h_{T_{ref}}^0$  the enthalpy of formation of the chemical specie involved, evaluated at the reference temperature  $T_{ref} = 0$  K. Assuming the reference scales provided in Section 2.1, after some manipulations Eqs. (2)–(5) can be recast in non-dimensional form:

$$\frac{\partial \rho}{\partial t} + \nabla \cdot (\rho \mathbf{u}) = 0, \quad (A.3)$$

$$\frac{\partial (\rho \mathbf{u})}{\partial t} + \nabla \cdot (\rho \mathbf{u} \otimes \mathbf{u}) = \frac{1}{Re} \nabla \cdot \boldsymbol{\tau} - \frac{1}{Ma^2} \nabla p + \frac{\mathbf{f}_\sigma}{We} + \frac{\rho \mathbf{g}}{Fr^2}, \quad (A.4)$$

$$\frac{\partial (\rho e)}{\partial t} + \nabla \cdot (\rho \mathbf{u} e) + Ma^2 \left[ \frac{\partial}{\partial t} \left( \rho \frac{\mathbf{u} \cdot \mathbf{u}}{2} \right) + \nabla \cdot \left( \rho \frac{\mathbf{u} \cdot \mathbf{u}}{2} \right) \right] = \quad (A.5)$$

$$\begin{aligned} & \frac{\gamma}{\gamma - 1} \frac{1}{Re Pr} \nabla \cdot (k \nabla T) - \nabla \cdot (\mathbf{u} p) \\ & + Ma^2 \left[ \frac{1}{Re} \nabla \cdot (\boldsymbol{\tau} \cdot \mathbf{u}) + \frac{\mathbf{f}_\sigma}{We} + \frac{\rho \mathbf{g}}{Fr^2} \right] \cdot \mathbf{u}, \\ p & = \Pi \rho T. \end{aligned} \quad (A.6)$$

where  $Ma = \tilde{U} / \sqrt{\tilde{p}/\tilde{\rho}}$  is a pseudo-Mach number, whereas the definition of all the other parameters can be found in Section 2.1. The low-Mach number limit of Eqs. (A.3)–(A.6) can be derived from a single-scale asymptotic expansion in the limit of small Mach numbers [44]. Since the pseudo Mach number,  $Ma$ , appears in all the equations only with the power of two, each generic vectorial and scalar quantity,  $\mathbf{f}$ , can be expanded in the following way:

$$\mathbf{f}(\mathbf{x}, t) = \mathbf{f}_0(\mathbf{x}, t) + \mathbf{f}_2(\mathbf{x}, t) Ma^2 + O(Ma^3). \quad (A.7)$$

It is also possible to prove that the following relations hold for the product of two scalar quantities:

$$[f(\mathbf{x}, t)g(\mathbf{x}, t)]_0 = f_0(\mathbf{x}, t)g_0(\mathbf{x}, t), \quad (A.8)$$

$$[f(\mathbf{x}, t)g(\mathbf{x}, t)]_2 = f_2(\mathbf{x}, t)g_0(\mathbf{x}, t) + f_0(\mathbf{x}, t)g_2(\mathbf{x}, t). \quad (A.9)$$

To obtain the low-Mach number limit of the momentum equation, Eq. (A.4), we use the asymptotic expansion provided by Eq. (A.7) into Eq. (A.4):

$$\begin{aligned} & \frac{\partial}{\partial t} [(\rho \mathbf{u})_0 + (\rho \mathbf{u})_2 Ma^2 + O(Ma^3)] \\ & + \nabla \cdot [(\rho \mathbf{u} \otimes \mathbf{u})_0 + (\rho \mathbf{u} \otimes \mathbf{u})_2 Ma^2 + O(Ma^3)] \\ & = \frac{1}{Re} \nabla \cdot [\boldsymbol{\tau}_0 + \boldsymbol{\tau}_2 Ma^2 + O(Ma^3)] \\ & - \frac{1}{Ma^2} \nabla [p_0 + p_2 Ma^2 + O(Ma^3)] + \\ & + \frac{1}{We} [\mathbf{f}_{\sigma 0} + \mathbf{f}_{\sigma 0} Ma^2 + O(Ma^3)] \\ & + \frac{1}{Fr} [(\rho \mathbf{g})_0 + (\rho \mathbf{g})_2 Ma^2 + O(Ma^3)]. \end{aligned} \quad (A.10)$$

Multiplying by  $Ma^2$  and collecting all terms of same order in  $Ma$  in Eq. (A.10), leads, after some manipulation, to the zeroth-order equation,

$$\nabla p_0 = 0, \quad (A.11)$$

and to the second-order relation,

$$\frac{\partial \mathbf{u}_0}{\partial t} + \mathbf{u}_0 \cdot \nabla \mathbf{u}_0 = \frac{1}{\rho_0} \left[ \frac{1}{Re} \nabla \cdot \boldsymbol{\tau}_0 - \nabla p_2 + \frac{\mathbf{f}_{\sigma 0}}{We} \right] + \frac{\mathbf{g}}{Fr^2}. \quad (A.12)$$

The algebraic manipulations for the continuity and energy equations are completely omitted due to their similarity with the procedure described above for the momentum equation. The reader is referred to the following references [43,44,74] for additional details. The final low-Mach number equations can be written as:

$$\frac{\partial \rho_0}{\partial t} + \nabla \cdot (\rho_0 \mathbf{u}_0) = 0, \quad (\text{A.13})$$

$$\frac{\partial \mathbf{u}_0}{\partial t} + \mathbf{u}_0 \cdot \nabla \mathbf{u}_0 = \frac{1}{\rho_0} \left[ \frac{1}{Re} \nabla \cdot \boldsymbol{\tau}_0 - \nabla p_2 + \frac{\mathbf{f}_{\sigma 0}}{We} \right] + \frac{\mathbf{g}}{Fr^2}, \quad (\text{A.14})$$

$$\frac{\partial (\rho_0 e_0)}{\partial t} + \nabla \cdot (\rho_0 \mathbf{u}_0 e_0) = \frac{\gamma}{\gamma - 1} \frac{1}{RePr} \nabla \cdot (k \nabla T_0) - \nabla \cdot (p_0 \mathbf{u}), \quad (\text{A.15})$$

$$p_0 = \Pi \rho_0 T_0. \quad (\text{A.16})$$

It should be noted that, in the limit of small Mach number, the contribution of the viscous dissipation to the overall energy balance of the gaseous flow does not appear in Eq. (A.15). This holds true under the hypothesis of sufficiently high Reynolds number. In fact, the term  $\nabla \cdot (\boldsymbol{\tau} \cdot \mathbf{u})$  in Eq. (A.5), which is pre-multiplied by the factor  $Ma^2/Re$ , may become significant in the limit of Mach tending to zero for sufficiently low Reynolds number. The effect of the viscous dissipation could be easily included in the equations above; however we consider here high Reynolds number flows for the gas phase, for which Eq. (A.15) is an accurate approximation. The subscript referring to the order of quantities are omitted in this manuscript, except for the pressure terms. It is useful to remind that, for the chosen set of reference scales, the non-dimensional sensible energy reads:  $e = 1/(\gamma - 1)\Pi T$ . Considering the latter and Eq. (A.16), after some additional manipulations, Eqs. (A.13)–(A.16) can be recast as Eqs. (8)–(12) provided in Section 2.1.

## References

- [1] Hirt CW, Nichols BD. Volume of fluid (VOF) method for the dynamics of free boundaries. *J Comput Phys* 1981;39(1):201–25.
- [2] Elghobashi S. Direct numerical simulation of turbulent flows laden with droplets or bubbles. *Annu Rev Fluid Mech* 2019;51:217–44.
- [3] Tanguy S, Sagan M, Lalanne B, Couderc F, Colin C. Benchmarks and numerical methods for the simulation of boiling flows. *J Comput Phys* 2014;264:1–22.
- [4] Le Martelot S, Saurel R, Nkongha B. Towards the direct numerical simulation of nucleate boiling flows. *Int J Multiphase Flow* 2014;66:62–78.
- [5] Salvador F, Romero J, Roselló M, Jaramillo D. Numerical simulation of primary atomization in diesel spray at low injection pressure. *J Comput Appl Math* 2016;291:94–102.
- [6] Duret B, Reveillon J, Menard T, Demoulin F. Improving primary atomization modeling through DNS of two-phase flows. *Int J Multiphase Flow* 2013;55:130–7.
- [7] Picano F, Breugem WP, Brandt L. Turbulent channel flow of dense suspensions of neutrally buoyant spheres. *J Fluid Mech* 2015;764:463–87.
- [8] Balcázar N, Lehmkuhl O, Jofre L, Rigola J, Oliva A. A coupled volume-of-fluid/level-set method for simulation of two-phase flows on unstructured meshes. *Comput Fluids* 2016;124:12–29.
- [9] Cottet GH, Maitre E. A semi-implicit level set method for multiphase flows and fluid-structure interaction problems. *J Comput Phys* 2016;314:80–92.
- [10] Ardekani M, Rosti M, Brandt L. Turbulent flow of finite-size spherical particles in channels with viscous hyper-elastic walls. *J Fluid Mech* 2019;873:410–40.
- [11] Costa P, Picano F, Brandt L, Breugem WP. Effects of the finite particle size in turbulent wall-bounded flows of dense suspensions. *J Fluid Mech* 2018;843:450–78.
- [12] Rosti ME, De Vita F, Brandt L. Numerical simulations of emulsions in shear flows. *Acta Mech* 2019;230(2):667–82.
- [13] Dalla Barba F, Picano F. Clustering and entrainment effects on the evaporation of dilute droplets in a turbulent jet. *Phys Rev Fluids* 2018;3(3):034304.
- [14] Rosti ME, Picano F, Brandt L. Numerical approaches to complex fluids. In: *Flowing matter*. Springer; 2019. p. 1–34.
- [15] Hirt CW, Amsden AA, Cook J. An arbitrary Lagrangian-Eulerian computing method for all flow speeds. *J Comput Phys* 1974;14(3):227–53.
- [16] Hughes TJ, Liu WK, Zimmermann TK. Lagrangian-Eulerian finite element formulation for incompressible viscous flows. *Comput Methods Appl Mech Eng* 1981;29(3):329–49.
- [17] Ganesan S, Tobiska L. Arbitrary Lagrangian-Eulerian finite-element method for computation of two-phase flows with soluble surfactants. *J Comput Phys* 2012;231(9):3685–702.
- [18] Unverdi SO, Tryggvason G. A front-tracking method for viscous, incompressible, multi-fluid flows. *J Comput Phys* 1992;100(1):25–37.
- [19] Peskin CS. Flow patterns around heart valves: a numerical method. *J Comput Phys* 1972;10(2):252–71.
- [20] Breugem WP. A second-order accurate immersed boundary method for fully resolved simulations of particle-laden flows. *J Comput Phys* 2012;231(13):4469–98.
- [21] Mittal R, Iaccarino G. Immersed boundary methods. *Annu Rev Fluid Mech* 2005;37:239–61.
- [22] Haeri S, Shrimpton J. On the application of immersed boundary, fictitious domain and body-conformal mesh methods to many particle multiphase flows. *Int J Multiphase Flow* 2012;40:38–55.
- [23] Kempe T, Fröhlich J. An improved immersed boundary method with direct forcing for the simulation of particle laden flows. *J Comput Phys* 2012;231(9):3663–84.
- [24] Sussman M, Ohta M. A stable and efficient method for treating surface tension in incompressible two-phase flow. *SIAM J Sci Comput* 2009;31(4):2447–71.
- [25] Sussman M, Smereka P, Osher S. A level set approach for computing solutions to incompressible two-phase flow. *J Comput Phys* 1994;114(1):146–59.
- [26] Osher S, Sethian JA. Fronts propagating with curvature-dependent speed: algorithms based on Hamilton-Jacobi formulations. *J Comput Phys* 1988;79(1):12–49.
- [27] Gibou F, Fedkiw R, Osher S. A review of level-set methods and some recent applications. *J Comput Phys* 2018;353:82–109.
- [28] Sethian JA, Smereka P. Level set methods for fluid interfaces. *Annu Rev Fluid Mech* 2003;35(1):341–72.
- [29] Scardovelli R, Zaleski S. Direct numerical simulation of free-surface and interfacial flow. *Annu Rev Fluid Mech* 1999;31(1):567–603.
- [30] Gueyffier D, Li J, Nadim A, Scardovelli R, Zaleski S. Volume-of-fluid interface tracking with smoothed surface stress methods for three-dimensional flows. *J Comput Phys* 1999;152(2):423–56.
- [31] O'Brien A, Bussmann M. A volume-of-fluid ghost-cell immersed boundary method for multiphase flows with contact line dynamics. *Comput Fluids* 2018;165:43–53.
- [32] Aulisa E, Manservigi S, Scardovelli R, Zaleski S. A geometrical area-preserving volume-of-fluid advection method. *J Comput Phys* 2003;192(1):355–64.
- [33] Xiao F, Honma Y, Kono T. A simple algebraic interface capturing scheme using hyperbolic tangent function. *Int J Numer Methods Fluids* 2005;48(9):1023–40.
- [34] Li S, Sugiyama K, Takeuchi S, Takagi S, Matsumoto Y, Xiao F. An interface capturing method with a continuous function: the THINC method with multi-dimensional reconstruction. *J Comput Phys* 2012;231(5):2328–58.
- [35] Pirozzoli S, Di Giorgio S, Iafrafi A. On algebraic TVD-VOF methods for tracking material interfaces. *Comput Fluids* 2019;189:73–81.
- [36] Pelanti M. Low mach number preconditioning techniques for Roe-type and HLLC-type methods for a two-phase compressible flow model. *Appl Math Comput* 2017;310:112–33.
- [37] Haimovich O, Frankel SH. Numerical simulations of compressible multicomponent and multiphase flow using a high-order targeted ENO (TEN0) finite-volume method. *Comput Fluids* 2017;146:105–16.
- [38] Lunati I, Jenny P. Multiscale finite-volume method for compressible multiphase flow in porous media. *J Comput Phys* 2006;216(2):616–36.
- [39] Saurel R, Lemetayer O. A multiphase model for compressible flows with interfaces, shocks, detonation waves and cavitation. *J Fluid Mech* 2001;431:239–71.
- [40] Saurel R, Abgrall R. A multiphase Godunov method for compressible multifluid and multiphase flows. *J Comput Phys* 1999;150(2):425–67.
- [41] Colella P, Pao K. A projection method for low speed flows. *J Comput Phys* 1999;149(2):245–69.
- [42] Wall C, Pierce CD, Moin P. A semi-implicit method for resolution of acoustic waves in low mach number flows. *J Comput Phys* 2002;181(2):545–63.
- [43] Müller B. Low-Mach-number asymptotics of the Navier-Stokes equations. *J Eng Math* 1998;34:97–109.
- [44] Majda A, Sethian J. The derivation and numerical solution of the equations for zero mach number combustion. *Combust Sci Technol* 1985;42(3–4):185–205.
- [45] Brackbill JU, Kothe DB, Zemach C. A continuum method for modeling surface tension. *J Comput Phys* 1992;100(2):335–54.
- [46] Rosti ME, Brandt L. Numerical simulation of turbulent channel flow over a viscous hyper-elastic wall. *J Fluid Mech* 2017;830:708–35.
- [47] Rosti ME, Brandt L, Mitra D. Rheology of suspensions of viscoelastic spheres: deformability as an effective volume fraction. *Phys Rev Fluids* 2018;3(1):012301.
- [48] Rosti ME, Ge Z, Jain SS, Dodd MS, Brandt L. Droplets in homogeneous shear turbulence. *J Fluid Mech* 2019;876:962–84. doi:10.1017/jfm.2019.581.
- [49] Battista F, Picano F, Casciola CM. Turbulent mixing of a slightly supercritical van der Waals fluid at low-Mach number. *Phys Fluids* 2014;26(5):055101.
- [50] Daru V, Le Quére P, Duluc M-C, Le Maitre O. A numerical method for the simulation of low mach number liquid-gas flows. *J Comput Phys* 2010;229(23):8844–67.
- [51] De Vita F, Rosti ME, Caserta S, Brandt L. Numerical simulations of vorticity banding of emulsions in shear flows. *Soft Matter* 2020.
- [52] De Vita F, Rosti ME, Caserta S, Brandt L. On the effect of coalescence on the rheology of emulsions. *J Fluid Mech* 2019;880:969–91.

- [53] Puckett EG, Almgren AS, Bell JB, Marcus DL, Rider WJ. A high-order projection method for tracking fluid interfaces in variable density incompressible flows. *J Comput Phys* 1997;130(2):269–82.
- [54] Scapin N, Costa P, Brandt L. A volume-of-fluid method for interface-resolved simulations of phase-changing two-fluid flows. *J Comput Phys* 2020:109251.
- [55] Castro M, Costa B, Don WS. High order weighted essentially non-oscillatory WENO-Z schemes for hyperbolic conservation laws. *J Comput Phys* 2011;230(5):1766–92.
- [56] Motheau E, Abraham J. A high-order numerical algorithm for DNS of low-mach-number reactive flows with detailed chemistry and quasi-spectral accuracy. *J Comput Phys* 2016;313:430–54.
- [57] Demou A, Frantzis C, Grigoriadis D. A low-mach methodology for efficient direct numerical simulations of variable property thermally driven flows. *Int J Heat Mass Transf* 2019;132:539–49.
- [58] Youngs DL. Time-dependent multi-material flow with large fluid distortion. *Numer Methods Fluid Dyn* 1982.
- [59] Youngs DL. An interface tracking method for a 3D Eulerian hydrodynamics code. Technical Report 44/92/35. Atomic Weapons Research Establishment (AWRE); 1984.
- [60] Costa P. A FFT-based finite-difference solver for massively-parallel direct numerical simulations of turbulent flows. *Comput Math Appl* 2018;76(8):1853–62.
- [61] Wilhelmson RB, Ericksen JH. Direct solutions for Poisson's equation in three dimensions. *J Comput Phys* 1977;25(4):319–31.
- [62] Schumann U, Sweet RA. Fast Fourier transforms for direct solution of Poisson's equation with staggered boundary conditions. *J Comput Phys* 1988;75(1):123–37.
- [63] Li N, Laizet S. 2DECOMP & FFT-a highly scalable 2D decomposition library and FFT interface. In: Cray user group 2010 conference; 2010. p. 1–13.
- [64] Bartholomew P, Laizet S. A new highly scalable, high-order accurate framework for variable-density flows: application to non-Boussinesq gravity currents. *Comput Phys Commun* 2019;242:83–94.
- [65] Dodd MS, Ferrante A. A fast pressure-correction method for incompressible two-fluid flows. *J Comput Phys* 2014;273:416–34.
- [66] Kang M, Fedkiw RP, Liu X-D. A boundary condition capturing method for multiphase incompressible flow. *J Sci Comput* 2000;15(3):323–60.
- [67] Hysing S-R, Turek S, Kuzmin D, Parolini N, Burman E, Ganesan S, et al. Quantitative benchmark computations of two-dimensional bubble dynamics. *Int J Numer Methods Fluids* 2009;60(11):1259–88.
- [68] Zayernouri M, Metzger M. Coherent features in the sensitivity field of a planar mixing layer. *Phys Fluids* 2011;23(2):025105.
- [69] Betchov R, Szewczyk A. Stability of a shear layer between parallel streams. *Phys Fluids* 1963;6(10):1391–6.
- [70] Lu J, Tryggvason G. Numerical study of turbulent bubbly downflows in a vertical channel. *Phys Fluids* 2006;18(10):103302.
- [71] Lu J, Tryggvason G. Effect of bubble deformability in turbulent bubbly upflow in a vertical channel. *Phys Fluids* 2008;20(4):040701.
- [72] Henningson DS, Kim J. On turbulent spots in plane poiseuille flow. *J Fluid Mech* 1991;228:183–205.
- [73] Costa P, Phillips E, Brandt L, Fatica M. GPU acceleration of CaNS for massively-parallel direct numerical simulations of canonical fluid flows. *Comput Math Appl* 2020. doi:10.1016/j.camwa.2020.01.002.
- [74] Meister A. Asymptotic single and multiple scale expansions in the low mach number limit. *SIAM J Appl Math* 1999;60(1):256–71.